

# Comparative assessment of drought monitoring indices susceptibility using geospatial techniques

Hui Yue (✉ [13720559861@163.com](mailto:13720559861@163.com))

Xi'an University of Science and Technology

Ying Liu

Xi'an University of Science and Technology

Jiixin Qian

Xi'an University of Science and Technology

---

## Research Article

**Keywords:** drought monitoring indices, gradient-based structural similarity (GSSIM), comparative assessment, SMMI/MSMMI, PDI/MPDI, geospatial techniques

**Posted Date:** March 1st, 2021

**DOI:** <https://doi.org/10.21203/rs.3.rs-174743/v1>

**License:**   This work is licensed under a Creative Commons Attribution 4.0 International License.

[Read Full License](#)

---

**Version of Record:** A version of this preprint was published at Environmental Science and Pollution Research on March 20th, 2021. See the published version at <https://doi.org/10.1007/s11356-021-13275-0>.

# 1 Comparative assessment of drought monitoring indices 2 susceptibility using geospatial techniques

3 Hui Yue, Ying Liu, Jiaxin Qian

4 *Xi'an University of Science and Technology, College of Geomatics, Yanta Road, Xi'an, China, 710054;*

5 \* Correspondence: 13720559861@163.com

6 **Abstract:** There are two main categories of dryness monitoring indices based on spectral feature space. One  
7 category uses the vertical distance from any point to a line passing through the coordinate origin, which is  
8 perpendicular to a soil line, to monitor the dryness conditions. The most popular indices are the Perpendicular  
9 Dryness Index (PDI) and the modified perpendicular dryness index (MPDI). The other category uses the distance  
10 from any point in feature space to the coordinate origin to represent the dryness status, for instance, the soil  
11 moisture (SM) monitoring index (SMMI) and the modified soil moisture monitoring index (MSMMI). In this study,  
12 the performances and differences of these four indicators were evaluated using field-measured SM (FSM) data  
13 based on Gaofen-1 (GF-1) wide field of view (WFV), Landsat-8 Operational Land Imager (OLI), and Sentinel-2  
14 Multi-Spectral Instrument (MSI) sensors. Performance evaluations were conducted in two study areas, namely an  
15 arid and semi-arid region of northwest China and a humid agricultural region of southwest Canada. We employed  
16 gradient-based structural similarity (GSSIM) to quantitatively assess the similarity of the structural information  
17 and structural characteristics among these four indicators. Monitoring SM in bare soil or low vegetation-covered  
18 areas in the semi-arid region, the SMMI, PDI, MSMMI, and MPDI from Near-infrared (NIR)-Red had significantly  
19 negative linear correlations with the FSM at 0-5 cm depth ( $P < 0.01$ ). However, SMMI was better than PDI in  
20 estimating SM in bare soil, which was better than MSMMI and MPDI for GF-1. Moreover, the PDI and SMMI  
21 had similar SM evaluation abilities, which were better than those of MPDI and MSMMI for Landsat-8. The GSSIM  
22 map of the SMMI/PDI and the MSMMI/MPDI showed that the low change areas accounted for 99.89% and 98.89%  
23 for GF-1, respectively, and 95.78% and 94.45% for Landsat-8, respectively. This result indicated that the SMMI,

24 PDI, MSMMI, and MPDI values from NIR-Red in low vegetation cover were similar. In monitoring SM in  
25 agricultural vegetation areas, the accuracy of the four indices from Short-wave Infrared (SWIR) feature space was  
26 higher than that from NIR-Red feature space for Sentinel-2. The SM monitoring effect of MSMMI and MPDI was  
27 better than that of SMMI and PDI. Due to the lack of SWIR band, GF-1 was limited in monitoring SM in  
28 vegetation-covered areas. The SMMI and MSMMI, which do not rely on the soil line, were more suitable than  
29 PDI and MPDI for retrieving SM in the complex surface environment depending on the soil line and the number  
30 of parameters. GF-1 with 16 m resolution had higher accuracy in SM assessment than Landsat-8 with 30 m  
31 resolution and had almost the same accuracy as Sentinel-2 with 20 m.

32 **Keywords:** drought monitoring indices; gradient-based structural similarity (GSSIM); comparative assessment;  
33 SMMI/MSMMI, PDI/MPDI; geospatial techniques

## 34 **1. Introduction**

35 Drought is a worldwide natural disaster period, and the frequency and intensity of drought have increased  
36 over the past 30 years (Shahabfar et al. 2012). Drought can generate many environmental, societal, and economic  
37 issues, especially in agricultural regions (Zhang et al. 2017). Remote sensing technology is one of the most efficient  
38 approaches for monitoring dryness across large areas (Ghulam et al. 2007b). Based on various types of remote  
39 sensing data, numerous dryness indicators have been proposed. For instance, these indicators include the  
40 vegetation condition index (VCI) (Kogan 1995a; Dutta et al. 2015), Normalized Difference Vegetation Index  
41 (NDVI) (Rouse et al. 1974), Temperature Condition Index (TCI) (Kogan 1995b; Singh et al. 2003), Temperature  
42 Vegetation Dryness Index (TVDI) (Sandholt et al. 2002; Liu et al. 2015; Liu and Yue 2018), thermal inertia (Price  
43 1985; Kang et al. 2017), indices based on Near Infrared (NIR)-Red space (Ghulam et al. 2007b; Liu et al. 2013;  
44 Amani et al. 2017) and microwave methods (Alizadeh and Nikoo 2018; Sawada 2018). These dryness indices  
45 involve visible wavelengths, NIR bands, thermal infrared bands, and microwave wavelengths. The methods based  
46 on spectral feature space are widely adopted to evaluate dryness or soil moisture conditions due to their clear

47 biophysical connotation, ease of acquisition, and operation.

48 In 1977, Richardson designed a Perpendicular Vegetation Index (PVI) based on a soil line in NIR-Red space.  
49 Zhan et al. (2007) constructed the soil moisture monitoring by remote sensing (SMMRS) model based on NIR-  
50 Red space to monitor soil moisture at depths of 5 cm and 0-20 cm. Ghulam et al. (2007a) applied the perpendicular  
51 distance from any point E in NIR-Red space to a line L, which passed through the coordinate origin and was  
52 vertical to the soil line, to represent the dryness conditions and named this index the Perpendicular Dryness Index  
53 (PDI). This index is more suitable for dryness monitoring in bare soil areas or areas with low vegetation cover but  
54 performs poorly in areas with high vegetation coverage. Then, Ghulam et al. (2007b) established a Modified  
55 Perpendicular Dryness Index (MPDI) in NIR-Red space by considering the influence of soil moisture and  
56 vegetation growth. Subsequently, a set of studies was carried out to validate these two indices and assess dryness  
57 or soil moisture conditions. Qin et al. (2008) showed that the PDI could estimate the dryness conditions in north-  
58 western China. The PDI and MPDI were adopted to evaluate the dryness conditions and the hydrological  
59 repartitioning and shifts in Iran (Shahabfar et al. 2011; Shahabfar and Eitzinger 2012; Shahabfar et al. 2014). Chen  
60 et al. (2015) employed the PDI and MPDI to verify the capability of Gaofen-1 (GF-1) wide field of view (WFV)  
61 sensors for monitoring soil moisture and indicated that the WFV sensor could be used to assess the status of the  
62 soil water content in Wuhan city. Zhang and Chen (2016) applied a satellite and in situ sensor collaborated  
63 reconstruction (SICR) method to reconstruct missing pixels contaminated by clouds and used the PDI and MPDI  
64 to evaluate the ability to use rebuilt GF-1 data for soil moisture inversion. Zormand et al. (2016) noted that the  
65 PDI, MPDI, and TVDI could all be used to map soil moisture in north-eastern Iran, and the MPDI was a suitable  
66 alternative to the standardized precipitation index (SPI) in agricultural dryness mapping. Comparisons between  
67 the VCI, TCI, PDI, MPDI, the precipitation condition index, and the soil moisture condition index showed that  
68 these indices had strengths and weaknesses in different climates across the continental United States (Zhang et al.

69 2017). Rao et al. (2017) indicated that there was a strong correlation between the MPDI and climatic water  
70 deficiency, which could be used to monitor the vegetation stress caused by dryness.

71 Numerous other dryness or soil moisture indices were proposed based on NIR-Red space or shortwave infrared1  
72 (SWIR1, band6)-shortwave infrared2 (SWIR2, band7) space of moderate-resolution imaging spectroradiometer  
73 (MODIS). Yao et al. (2011) adopted the distance between any point E and the coordinate origin O to represent the  
74 dryness status in SWIR1-SWIR2 of MODIS. Liu et al. (2013, 2017) used the distance, named the Soil Moisture  
75 Monitoring Index (SMMI), between any point E and the coordinate origin O to represent the soil moisture  
76 conditions in NIR-Red and compared it with the PDI. The results showed that these two indices could adequately  
77 assess soil moisture status. Li and Tan (2013) constructed the second MPDI (MPDI1), which combined PDI and  
78 PVI. Similar to the PDI, Dong et al. (2015) employed the perpendicular distance from any point E in the SWIR1-  
79 SWIR2 space of MODIS to a line L, which crossed the point (1,1) and was vertical to the soil line, to represent the  
80 dryness conditions. Chen et al. (2018) developed a new soil moisture index called the Normalized Soil Moisture  
81 Index (NSMI) in NIR-Red space, which was employed to downscale Soil Moisture Active Passive (SMAP)  
82 products from 36 km to 250 m resolution. Amani et al. (2017) transferred the NIR-Red spectral space to the soil  
83 moisture (SM)-PVI space, combined these data with the Land Surface Temperature (LST), and defined a new  
84 dryness index named the Temperature-vegetation-soil Moisture Dryness Index (TVMDI). Zhang et al. (2019)  
85 established a new dryness monitoring indicator called the Ratio Dryness Monitoring Index (RDMI) based on the  
86 wet edge, dry edge, and the soil line in NIR-Red space.

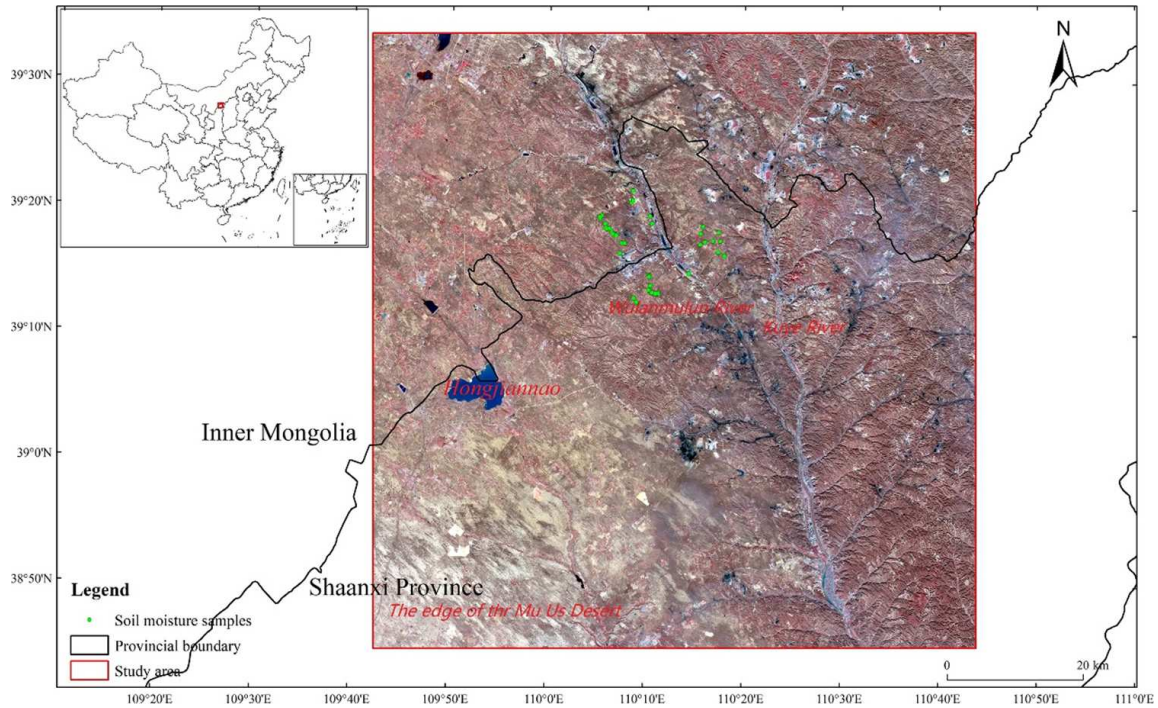
87 As shown above, we can see that the PDI, MPDI, TVMDI, and RDMI were designed based on the existing fixed  
88 soil line; however, the distribution of the soil line varies with soil type and soil fertilization, causing uncertainty in  
89 dryness assessments (Ghulam et al. 2007a; Qin et al. 2008; Yao et al. 2011). The SMMI is dependent on only the  
90 reflectance of the NIR and Red bands, which is not associated with fixed soil lines (Liu et al. 2013; Liu et al. 2017).

91 In this study, we will re-examine the potentials and the differences of the PDI, MPDI, SMMI, and a modified  
92 SMMI (MSMMI) in estimating SM in two cases. In Case I, these indices from NIR-Red feature space were firstly  
93 evaluated against in situ SM in the Shendong mining area based on a GF-1 WFV image with 16 m resolution and  
94 Landsat-8 Operational Land Imager (OLI) image with 30 m resolution. Secondly, the similarity of the structure  
95 information and structural characteristics among the PDI, MPDI, SMMI, and MSMMI were quantitatively  
96 measured by gradient-based structural similarity (GSSIM) (Liu et al. 2018). In Case II, these indices from NIR-  
97 Red feature space were firstly evaluated against the SMAPVEX SM data set in the Elm Creek and Carman,  
98 Manitoba, Canada based on a GF-1 WFV image with 16 m resolution and Sentinel-2 Multi-Spectral Instrument  
99 (MSI) image with 20 m resolution. Second, three additional feature spaces (Red-SWIR1, NIR-SWIR1, and  
100 SWIR1-SWIR2) from Sentinel-2 were constructed to estimate SM and compared with the NIR-Red space. Finally,  
101 we further evaluated the capability of GF-1 WFV and Sentinel-2 MSI sensors for estimating SM.

## 102 **2. Materials and Methodology**

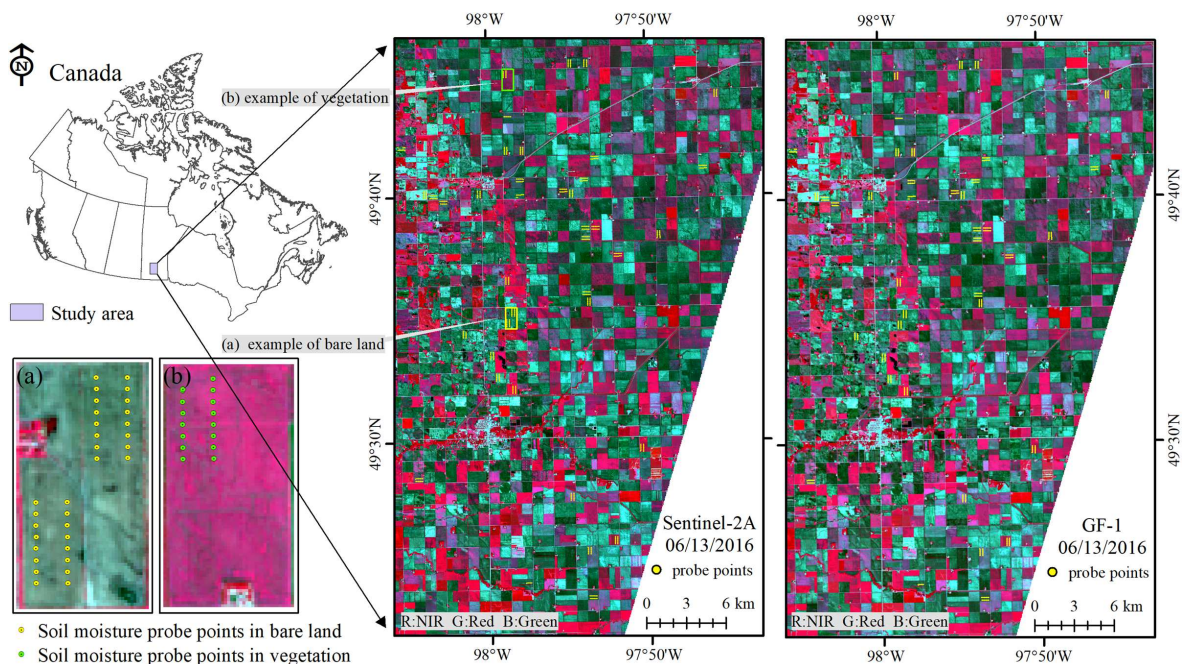
### 103 *2.1 Study areas*

104 Case 1: The Shendong mining area is one of the eight largest coalfields in the world, ranging from 38°52'N to  
105 39°41'N and from 109°51'E to 110°46'E. It is located in the south margin of the Mu Us desert and is adjacent to  
106 the north area of the Loess Plateau (Figure 1), which is famous for its lack of rain and serious soil erosion. The  
107 Shendong mining area is a typical arid and semi-arid desertification mining area in China. The average annual  
108 precipitation in this area is only 362 mm, and the evaporation is up to 2300 mm. The land desertification is severe  
109 in the study area with low vegetation coverage. In recent years, with the advancement of large-scale underground  
110 mining activities, a series of environmental problems, such as the drying up of wells, surface runoff reduction,  
111 water resource pollution, and groundwater level decline, have further aggravated the fragile ecological  
112 environment.



113  
114 **Fig.1.** Map of Shendong mining area in China

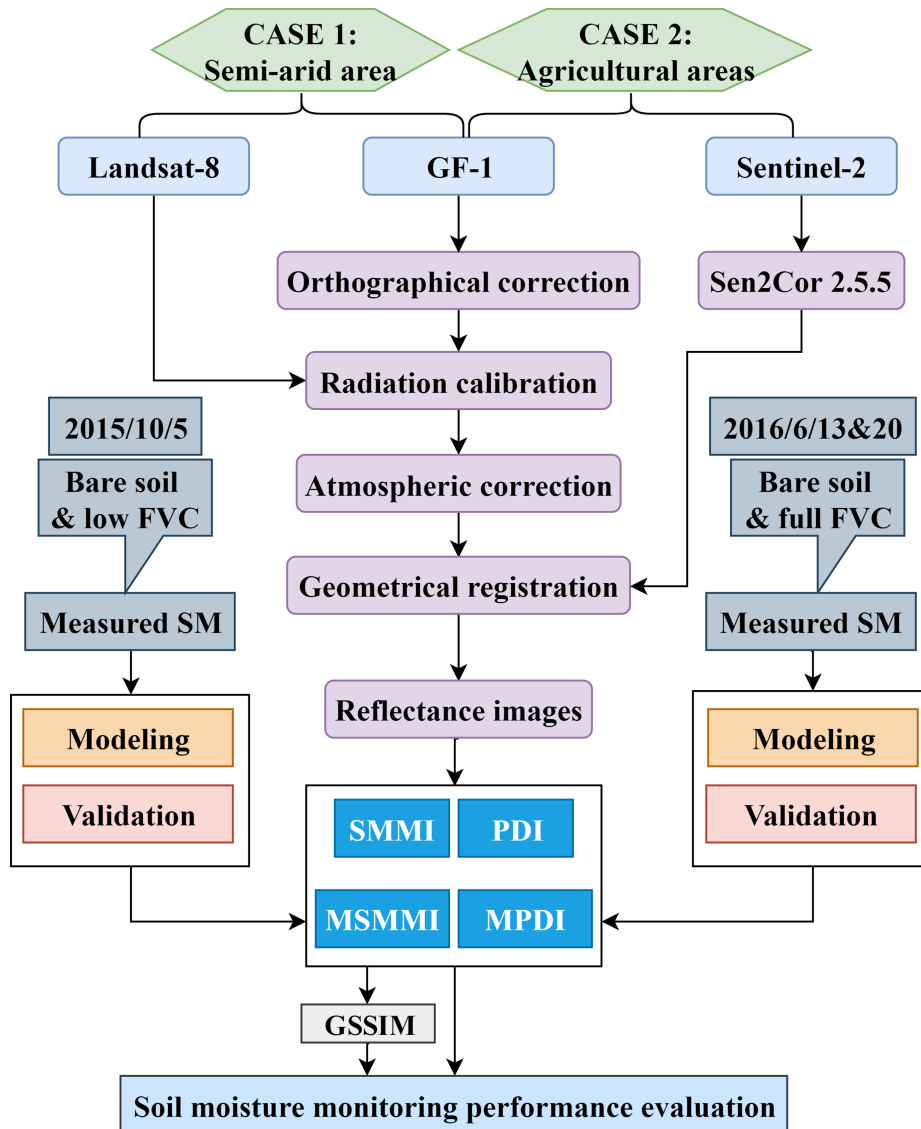
115 Case 2: The second study area locates in the Elm Creek and Carman, Manitoba, Canada with an area of 20 km  
116 × 30 km (Figure 2), ranging from 49°22'N to 49°46'N and from -98°5'E to -97°42'E. It is a typical temperate  
117 continental climate, with hot summer and sunny days, cold and long winter with sufficient sunshine. The terrain  
118 of the study area is flat and open. Barley, wheat, canola, soybean, and other cash crops are mainly cultivated in the  
119 study area.



120  
121 **Fig.2.** The geographic location of the SMAPVEX16 dataset in Canada

122 2.2 Data and pre-processing

123 The technical process (Figure 3) was divided into two parts according to the study areas.



124  
125 **Fig.3.** Technical process

126 Case I: A GF-1 image with 16 m resolution and Landsat-8 image with 30 m resolution on October 5, 2015, were  
 127 downloaded from the China Centre for Resources Satellite Data and Application ([CRSAC](http://www.cresda.com/CN/),  
 128 <http://www.cresda.com/CN/>) and the United States Geological Survey (<https://earthexplorer.usgs.gov/>),  
 129 respectively. The GF-1 satellite was the first satellite with a high-resolution earth observation system in China  
 130 (Chen et al. 2015). GF-1 was successfully launched on April 26, 2013, which opened the new era of China's Earth  
 131 observation. Two 2-m resolution panchromatic and 8-m resolution multispectral high-definition cameras, and four

132 16-m resolution wide-angle cameras were equipped on the GF-1 satellite. The GF-1 WFV sensor includes a blue  
133 band from 0.45~0.52  $\mu\text{m}$ , a green band from 0.52~0.59  $\mu\text{m}$ , a red band from 0.63~0.69  $\mu\text{m}$  and a NIR band from  
134 0.77~0.89  $\mu\text{m}$ . The pre-processing procedures, including radiometric calibration, atmospheric correction, ortho  
135 correction, and geometric registration, were executed in the Environment for Visualizing Image (ENVI).

136 We sampled on October 5, 2015, and acquired field-measured soil moisture (Figure 1). Samples were taken at  
137 depths of 0-5 cm and 10 cm, which were collected 2 to 3 times. The types of land cover were bare soil land or low  
138 vegetation-covered areas. The average relative soil moisture was derived by the traditional weighing method in  
139 the laboratory, which was dried for 12 hours at 105 °C.

140 Case II: Four Sentinel-2A L1C images on June 13 and 20, 2016 were derived from the European Space Agency  
141 (<https://scihub.copernicus.eu>). The image track number was 55 and the identification number was 14-UNV and  
142 UNV. Firstly, the Sen2Cor model (<http://step.esa.int/main/third-party-plugins-2/sen2cor/>) was used to perform  
143 atmospheric correction to obtain the real reflectance of each band. Secondly, mosaic and subset processing were  
144 carried out to obtain 20 m spatial resolution images (Mean synthesis) by Sentinel application platform (SNAP)  
145 (<http://step.esa.int/main/toolboxes/snap/>). The cloud mask file of the L2A product was applied for cloud removal  
146 of the image on June 20, 2016. GF-1 images on June 13 and 21, 2016 were derived from CRSAC.

147 Radiation calibration, atmospheric correction, ortho correction, and geometric registration were performed on  
148 GF-1 by ENVI. Finally, the real reflectance images with 16m spatial resolution were obtained.

149 In this study, field-measured SM data from the SMAPVEX16 dataset were employed to compare and analyze  
150 the relationship among the SMMI, PDI, MSMMI, and MPDI. Dataset was derived from earth data  
151 (<https://search.earthdata.nasa.gov>) (McNairn et al., 2018), which was designed to calibrate and improve the  
152 precision of NASA's soil moisture active and passive products (SMAP) (Entekhabi et al. 2010). The SM probe  
153 data was selected as the SM verification data, which measured the SM in 0-5cm depth. Each probe point measured

154 the top, middle, and bottom of the 0-5cm soil layer. Mean values of SM at three different depths were taken. The  
 155 measured SM points of FVC (Fractional vegetation cover)  $\leq 0.3$  were regarded as bare soil areas, and those of  
 156 FVC  $> 0.3$  were regarded as vegetation-covered areas. There were 200 measured SM points in bare soil areas (the  
 157 mean FVC was 0.065) on June 14, 2016. 140 points were randomly selected to establish the SM model in bare soil  
 158 areas. The remaining 60 points were adopted to test the estimation accuracy of the SM model. There were 195  
 159 measured SM points in vegetation-covered areas (the mean FVC was 0.522). 137 points and 58 points were  
 160 randomly selected to establish the SM model in vegetation-covered areas and test the accuracy, respectively. The  
 161 measured SM points on June 20, 2016, were used for correlation analysis with the four indexes. The number of  
 162 bare soil sample points and vegetation sample points was 147 and 51, respectively. Table 1 shows the vegetation  
 163 coverage condition of measured SM points in Case II.

164 **Table 1** The surface coverage of SM probe points in two periods of Case II

SM date Land cover type	14/6/2016		20/6/2016	
	NDVI <sub>m</sub>	FVC <sub>m</sub>	NDVI <sub>m</sub>	FVC <sub>m</sub>
Bare soil (FVC $\leq 0.30$ )	0.274	0.065	0.315	0.115
Vegetation (FVC $> 0.30$ )	0.743	0.522	0.786	0.646

165 Note: NDVI<sub>m</sub> and FVC<sub>m</sub> are the mean NDVI and FVC

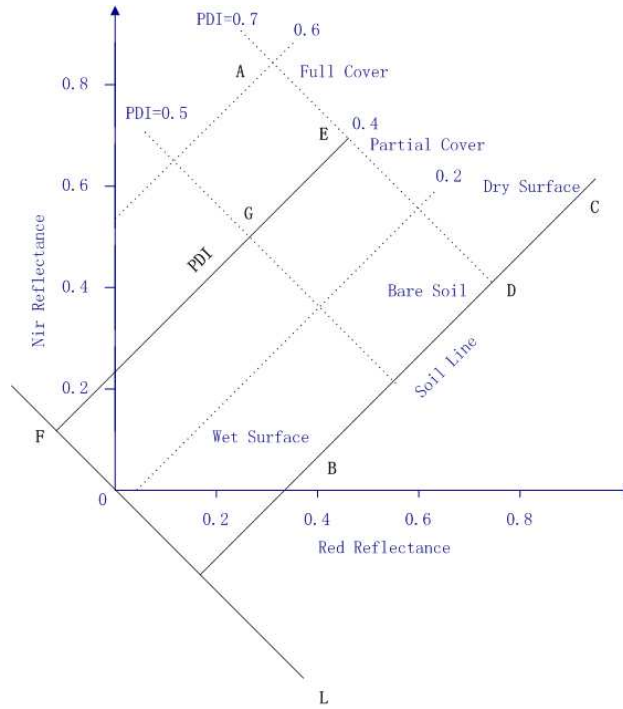
## 166 2.3 Methods

### 167 2.3.1 PDI and MPDI

168 In NIR-Red space, the perpendicular distance  $|EF|$  (Figure 4), which is called PDI, can reflect the dryness  
 169 conditions, which can be written as

$$170 \quad PDI = (R_{Red} + MR_{NIR}) / \sqrt{1 + M^2} \quad (1)$$

171 where  $R_{Red}$  and  $R_{NIR}$  are the reflectance of the Red and NIR bands, respectively. M represents the slope of  
 172 soil line BC (B represents the wet surface, C represents the dry surface). According to the distribution  
 173 characteristics of soil pixels in the NIR-Red space, the soil pixels constituting the soil line are often distributed at  
 174 the bottom of the scatter plot, that is, the point with the smallest NIR reflectance value corresponding to each red  
 175 reflectance value. Thus, we automatically obtained the value of M through MATLAB software.



176  
177 **Fig. 4.** Sketch map of PDI

178 Ghulam et al. (2007b) noted that the value of PDI was the same from points D and E to A (D represents bare  
179 soil, E represents partial cover, A represents full cover), indicating that the dryness conditions in areas with dry  
180 bare soil, partial vegetation coverage, and full vegetation coverage were identical. PDI does not involve the impacts  
181 of vegetation conditions and soil moisture status. Thus, considering the vegetation coverage (FVC), Ghulam et al.  
182 (2007b) developed a modified perpendicular dryness index (MPDI), which can be expressed as

$$183 \quad MPDI = \frac{R_{Red} + MR_{NIR} - FVC(R_{v,Red} + R_{v,NIR})}{(1 - FVC)\sqrt{1 + M^2}} \quad (2)$$

184 with

$$185 \quad FVC = 1 - \left( \frac{NDVI_{max} - NDVI}{NDVI_{max} - NDVI_{min}} \right)^{0.6715} \quad (3)$$

186 where  $R_{v,Red}$  and  $R_{v,NIR}$  are the reflectance of pure vegetation pixels in the red and NIR bands, respectively.  
187  $NDVI_{max}$  and  $NDVI_{min}$  represent the maximum and minimum values of NDVI, respectively.

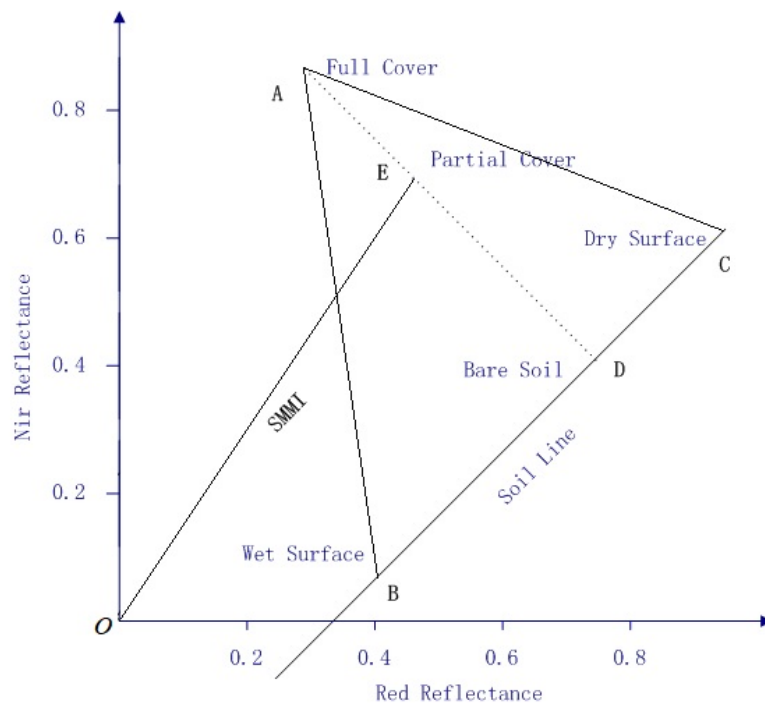
188 In the PDI and MPDI, the NIR or Red band could be replaced with SWIR1 and SWIR 2 to form the feature  
189 space of Red-SWIR1, NIR-SWIR1, or SWIR1-SWIR2 (Ghulam et al. 2007c, Yao et al. 2011). Correspondingly,  
190  $R_{v,SWIR1}$  and  $R_{v,SWIR2}$  are the reflectance of pure vegetation pixels in the SWIR1 and SWIR2 bands,  
191 respectively.

192 **2.3.2 SMMI and MSMMI**

193 In NIR-Red space, the distance between a black body, which is located at the coordinate origin O, and the origin  
 194 O is zero (0,0). The higher the soil moisture of any object with a certain reflective capacity is, the closer it is to the  
 195 origin O (Zhan et al. 2006). Liu et al. (2013, 2017) employed the distance  $|OE|$ , designated SMMI, to evaluate  
 196 the soil moisture status in NIR-red space (Figure 5), which can be calculated by

$$197 \quad SMMI = \sqrt{R_{Red}^2 + R_{NIR}^2} \quad (4)$$

198 A larger SMMI means that point E is far from point B and the soil moisture is smaller (A represents full cover,  
 199 B represents the wet surface, C represents the dry surface, D represents bare soil, E represents partial cover).



200  
 201 **Fig.5.** Sketch map of SMMI

202 SMMI also does not address the effect of vegetation coverage. Based on MPDI and FVC, this paper constructed  
 203 a modified soil moisture index (MSMMI), which can be written as

$$204 \quad MSMMI = \frac{\sqrt{(R_{Red}-FVC \cdot R_{v,Red})^2 + (R_{NIR}-FVC \cdot R_{v,NIR})^2}}{1 - FVC} \quad (5)$$

205 Similar to PDI and SMMI, red and NIR bands in MPDI and MSMMI can also be replaced by SWIR bands.

### 206 2.3.3 Feature space

207 Case I: Previous studies have shown that the NIR-Red feature space may not be the best space for monitoring  
 208 SM in vegetation-covered areas (Ghulam, 2007b). The surface cover type of all sample points in Case I was bare  
 209 soil land, so only the NIR-Red space was constructed to monitor the similarities and differences of soil moisture  
 210 by comparing Landsat data and GF-1 data. The FVC formula of GF-1 and Landsat8 was shown in formula (3). In

211 this study, the estimated values  $R_{v,Red}$  for GF-1 and Landsat-8 are 0.06 and 0.05, respectively. The estimated  
 212 values  $R_{v,NIR}$  for GF-1 and Landsat-8 are 0.12 and 0.20, respectively.

213 Case II: The land cover types of the sample points in Case II were vegetation and bare soil land. Several studies  
 214 showed that short-wave infrared band (SWIR) can effectively improve the accuracy of soil moisture estimation  
 215 (Ghulam et al. 2007c, Yao et al. 2011, Koley and Jeganathan, 2020). SMMI, PDI, MSMMI, and MPDI from NIR-  
 216 Red, Red-SWIR1, SWIR1-NIR, and SWIR1-SWIR2 feature spaces from Sentinel-2 were built. The FVC of  
 217 Sentinel-2 was extracted by the Biophysical Processor in SNAP software. The FVC formula of GF-1 was shown  
 218 in formula (3). The FVC of Sentinel-2 was extracted by the Biophysical Processor in SNAP. Because the GF-1  
 219 satellite lacks a SWIR band, only NIR-Red feature space was constructed. The estimated values  $R_{v,Red}$  for GF-  
 220 1 and Sentinel-2 are 0.03 and 0.03, respectively. The estimated values  $R_{v,NIR}$  for GF-1 and Sentinel-2 are 0.50  
 221 and 0.59, respectively. The estimated values of  $R_{v,SWIR1}$  and  $R_{v,SWIR2}$  for Sentinel-2 are 0.21 and 0.09,  
 222 respectively.

### 223 2.3.4 GSSIM

224 We adopted GSSIM to quantitatively measure the spatial similarity and distribution characteristics of SMMI,  
 225 MSMMI, PDI, and MPDI. Luminance comparison information  $l(x, y)$ , contrast comparison information  $c(x, y)$ ,  
 226 and gradient-based structure comparison information  $g(x, y)$  of the image constitutes GSSIM (Liu and Yue, 2018),  
 227 which was defined as

$$228 \quad GSSIM(x, y) = [I(x, y)]^\alpha [c(x, y)]^\beta [g(x, y)]^\gamma \quad (6)$$

229 with

$$230 \quad I(x, y) = \frac{2\mu_x\mu_y + c_1}{\mu_x^2 + \mu_y^2 + c_1} \quad (7)$$

$$231 \quad c(x, y) = \frac{2\sigma_x\sigma_y + c_2}{\sigma_x^2 + \sigma_y^2 + c_2} \quad (8)$$

$$232 \quad g(x, y) = \frac{2 \sum_j \sum_i G_x(i, j)G_y(i, j) + c_3}{\sum_j \sum_i [G_x(i, j)]^2 + \sum_j \sum_i [G_y(i, j)]^2 + c_3} \quad (9)$$

233 where  $\mu_x$  and  $\mu_y$  refer to the average of two images.  $\sigma_x$  and  $\sigma_y$  stand for the standard deviation of two images.  $G_x(i,$   
 234  $j)$  and  $G_y(i, j)$  are the gradient values of the pixel $_{(i,j)}$  of two images.  $c_1 = (K_1 L)^2$ ,  $c_2 = (K_2 L)^2$  and  $c_3 = c_2/2$  with  $K_1,$   
 235  $K_2 \leq 1$ , and  $L$  is the greyscale of an image. In this paper, the values of  $\alpha$ ,  $\beta$ , and  $\gamma$  were one. The values of  $c_1$  and  $c_2$

236 were 0.0001 and  $c_3$  equaled 0.0005 (Liu and Yue, 2018). The higher the value of GSSIM is, the more similar the  
 237 values of the two indicators are. This condition demonstrates that the ability of these two indices to monitor dryness  
 238 is analogous.

239 GSSIM can be categorized into three types (Liu and Yue, 2018): 1) high change ( $0 < \text{GSSIM} \leq 0.25$ ), exhibiting  
 240 that the values of the two indicators vary dramatically; 2) moderate change ( $0.25 < \text{GSSIM} \leq 0.65$ ), expressing that  
 241 the values of the two indicators change moderately; and 3) low change ( $0.65 < \text{GSSIM} \leq 1.0$ ), indicating that the  
 242 values of the two indicators are very similar.

### 243 2.3.4 Validation

244 We adopted field-measured SM samples to evaluate the performances of SMMI, MSMMI, PDI, and MPDI in  
 245 dryness monitoring. The field-measured SM samples were divided into two parts, one part for the linear  
 246 relationship construction, the other part for the SM inversion model's construction. First, we constructed linear  
 247 relationships between field-measured SM and these four indicators. Second, estimated soil moisture was derived  
 248 from the inversion models of the four indices, which were compared with the corresponding field-measured SM.  
 249 Finally, we employed the correlation coefficient (R), mean relative error (MRE), and root mean square error  
 250 (RMSE) to assess the accuracy of the inversion models of the four indicators. The expressions of R, MRE, and  
 251 RMSE can be described as:

$$252 \quad R = \frac{\sum_{i=1}^n (SM_{fi} - \overline{SM_f})(SM_{ei} - \overline{SM_e})}{\sqrt{\sum_{i=1}^n (SM_{fi} - \overline{SM_f})^2} \sqrt{\sum_{i=1}^n (SM_{ei} - \overline{SM_e})^2}} \quad (10)$$

$$253 \quad MRE = \frac{1}{n} \sum_{i=1}^n \frac{|SM_{fi} - SM_{ei}|}{SM_{fi}} \quad (11)$$

$$254 \quad RMSE = \sqrt{\frac{\sum_{i=1}^n (SM_{fi} - SM_{ei})^2}{n}} \quad (12)$$

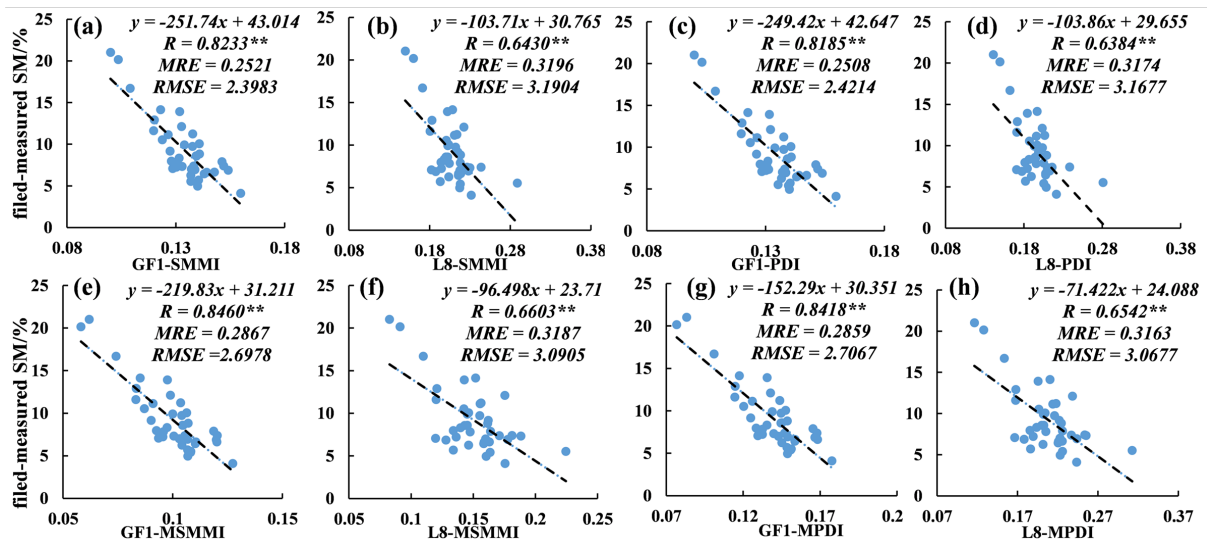
255 where  $SM_{fi}$  and  $\overline{SM_f}$  are the field-measured SM and the average of  $SM_{fi}$ , respectively.  $SM_{ei}$  and  $\overline{SM_e}$  are the  
 256 estimated SM and average of  $SM_{ei}$ , respectively.

257 We compared the results from GF-1 with those from Landsat-8 and Sentinel-2 to further assess the capacity of  
 258 GF-1 for estimating SM.

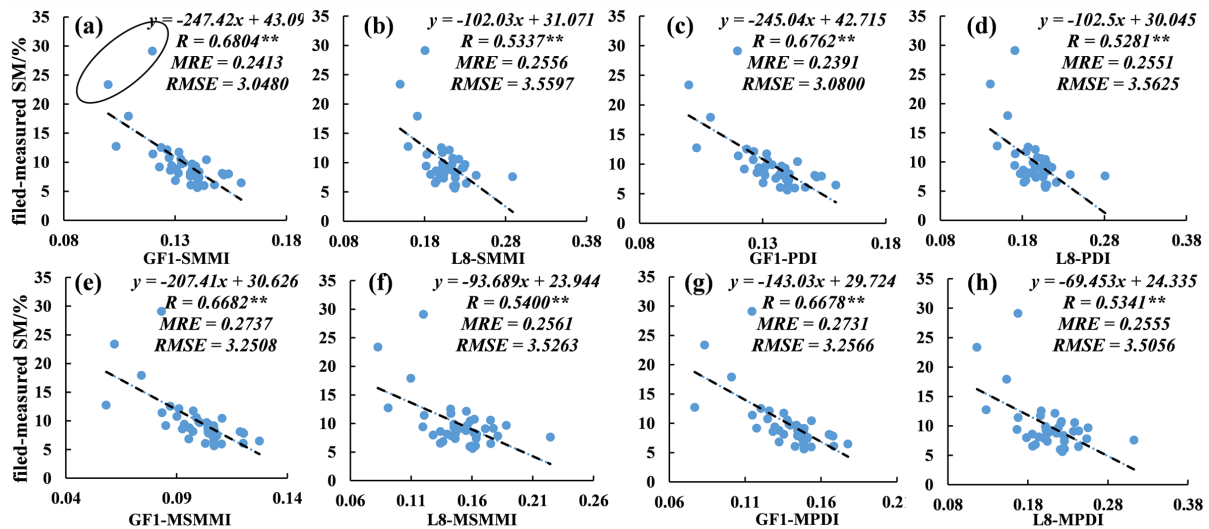
## 259 3. Results

260 3.1 Inversion model construction and evaluation: Case I

261 We established inversion models based on 40 samples of field-measured soil moisture (FSM) and SMMI,  
 262 MSMMI, PDI, and MPDI from GF-1 and Landsat-8 (L8). We applied the inversion models of the four indices to  
 263 estimate SM, which were compared with 17 samples using FSM. R, MRE, and RMSE to verify the accuracy of  
 264 the inversion models. Figures 6 and 7 show that all four indicators can assess the soil moisture at depths of 0-5 cm  
 265 and 10 cm. However, the negative linear relationship between the four indicators of GF-1 and L8 and FSM are  
 266 higher at the 0-5 cm depth than at the 10 cm depth. Figures 6 and 7 also indicate that the R between the four indices  
 267 of GF-1 and FSM is higher than that of L8. The R values between SMMI, PDI, and FSM at the 0-5 cm depth for  
 268 GF-1 are 0.8233 and 0.8185, which are higher than those for L8 (R values are 0.6430 and 0.6384, respectively).  
 269 The R values between MPDI and MSMMI and FSM at 0-5 cm depth for GF-1 are 0.8418 and 0.8460, respectively,  
 270 which are higher than those for L8 (R values are 0.6542 and 0.6603, respectively). The RMSE values between  
 271 SMMI, PDI, MPDI, and MSMMI and FSM at the 0-5 cm depth for GF-1 are 2.3983, 2.4214, 2.7067, and 2.6978,  
 272 respectively, which are lower than those for L8 (RMSEs are 3.1904, 3.1677, 3.0677 and 3.0905, respectively). A  
 273 small number of scattered points deviated from the fitting line of models, mainly because they were located in  
 274 low-lying areas with higher moisture in the deep soil (10cm). This also indicates that remote sensing monitoring  
 275 mainly reflects the surface soil moisture.

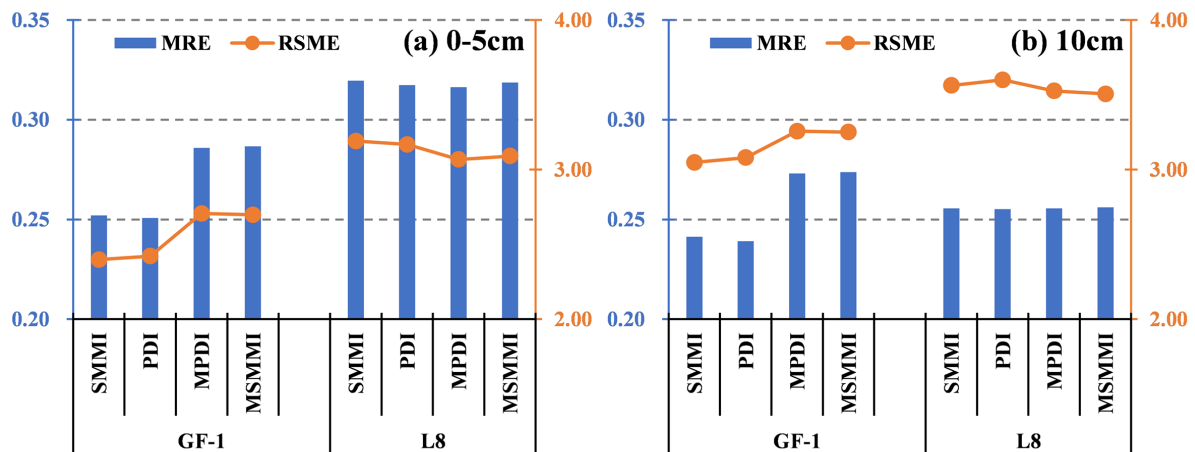


276  
 277 **Fig.6.** Relationship between four indicators and FSM in 0-5cm depth. (a) GF1-SMMI and FSM. (b) L8-SMMI  
 278 and FSM (c) GF1-PDI and FSM. (d) L8-PDI and FSM. (e) GF1-MSMMI and FSM. (f) L8-MSMMI and FSM.  
 279 (g) GF1-MPDI and FSM. (h) L8-MPDI and FSM.



280  
 281 **Fig.7.** Relationship between four indicators and FSM in 10cm depth. (a) GF1-SMMI and FSM. (b) L8-SMMI and  
 282 FSM (c) GF1-PDI and FSM. (d) L8-PDI and FSM. (e) GF1-MSMMI and FSM. (f) L8-MSMMI and FSM. (g)  
 283 GF1-MPDI and FSM. (h) L8-MPDI and FSM.

284 Figures 6, 7, and 8 also demonstrate that although the R values of the equations between MSMMI and MPDI  
 285 and FSM for GF-1 and L8 are slightly higher than those for SMMI and PDI and FSM, the MRE and RMSE  
 286 between the retrieved soil moisture and FSM for SMMI and PDI are lower than those for MSMMI and MPDI.  
 287 This result also indicates that GF-1, which has a higher resolution (16 m), exhibits better performance in  
 288 monitoring the soil moisture of the Shendong mining area than L8. In terms of soil moisture retrieval, SMMI is  
 289 better than PDI, which is better than MSMMI and MPDI for GF-1. PDI and SMMI have similar abilities to evaluate  
 290 soil moisture, which are slightly better than MPDI and MSMMI for L8. Although MPDI and MSMMI considered  
 291 the influence of vegetation, the Shendong mining area was vegetated but had low biomass due to the arid conditions,  
 292 which explained why MSMMI and MPDI performed less satisfactorily than SMMI and PDI. These conditions also  
 293 described why SMMI and PDI were more suitable for soil moisture assessment in bare soil areas or are with low  
 294 vegetation cover.



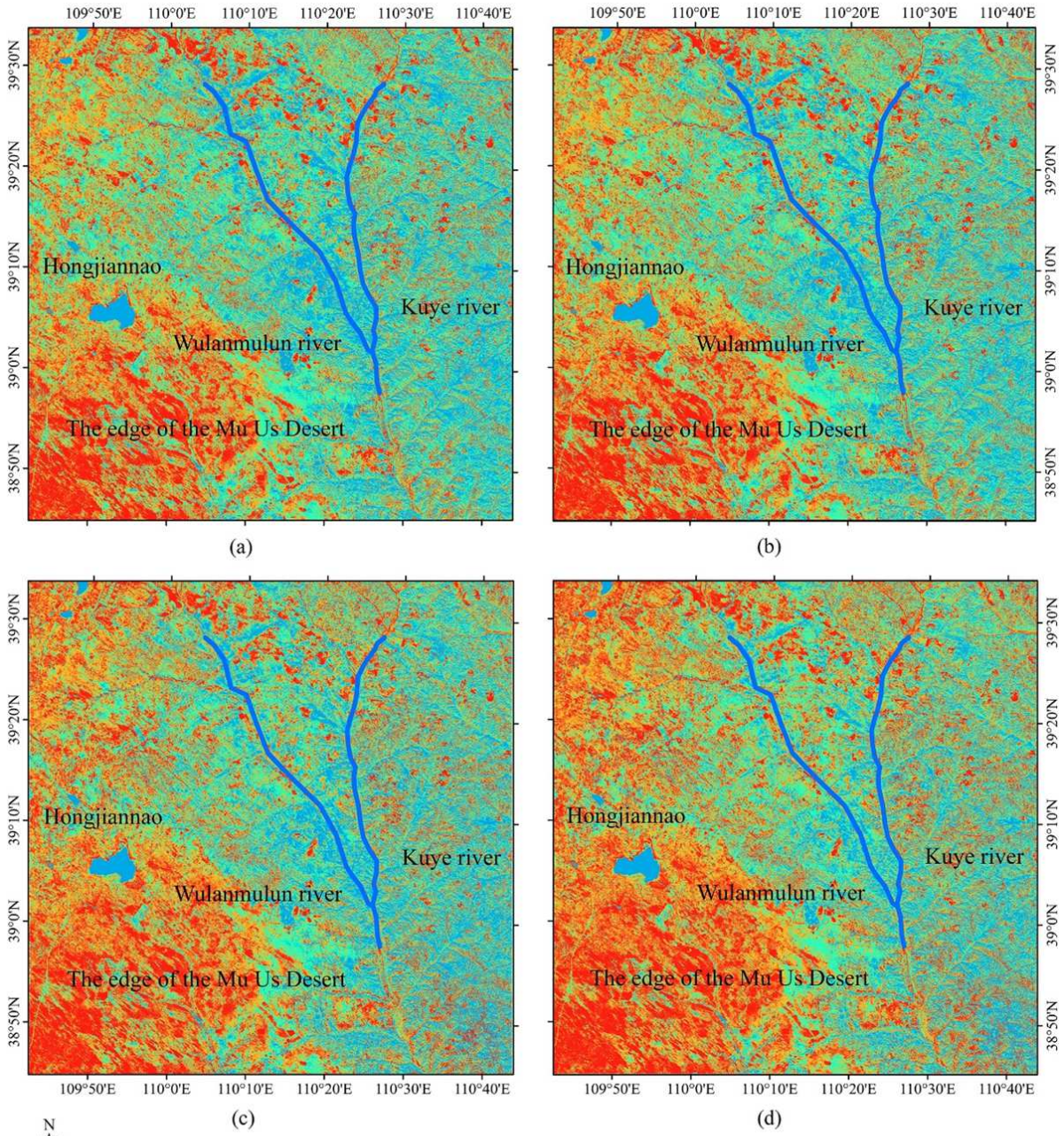
295  
 296 **Fig.8.** Accuracy of soil moisture estimation in 0-5cm and 10cm by GF-1 and L8.

297 3.1.1 The spatial distribution of SMMI, MSMMI, PDI, and MPDI

298 Due to the differences in the data ranges for SMMI, MSMMI, PDI, and MPDI, we need to rescale the values of  
 299 the four indices between 0 and 1. The closer the value is to 0, the higher the soil moisture is, and vice versa (Liu  
 300 et al. 2015). With an interval of 0.2, the levels of the four indicators were grouped into five categories: extremely  
 301 wet, wet, normal, dryness, and extreme dryness (Liu et al. 2015; Liu and Yue 2018). Figures 9 and 10 show that  
 302 the dryness status of the four indicators was very similar. The dryness and extreme dryness levels were located in  
 303 the north and northwest of the Shendong mining area and the edge of the Mu Us Desert, which accounted for  
 304 25.39%, 26.35%, 34.14%, and 30.18% of the areas when the SMMI, PDI, MPDI, and MSMMI of GF-1 were used,  
 305 respectively, while they accounted for 30.87%, 28.33%, 42.53% and 41.61% for L8 (Table 2). The wet and  
 306 extremely wet levels were located in the central and east of the Shendong mining area, which accounted for 50.31%,  
 307 48.97%, 39.13%, and 44.64% for the SMMI, PDI, MPDI, and MSMMI from GF-1, respectively, while they  
 308 accounted for 41.41%, 44.78%, 29.29% and 30.91% for L8. Figures 9 and 10 and Table 2 demonstrate that the  
 309 dryness status indicated by SMMI and PDI of GF-1 and L8 are very similar. Although the dryness conditions from  
 310 the MSMMI and MPDI from GF-1 and L8 were also similar, they were more severe than those from SMMI and  
 311 PDI. The percentages of the normal in the four indicators from GF-1, which all accounted for approximately 25%  
 312 of the area, were consistent with each other, which was smaller than that from L8.

313 **Table 2.** Percentage of dryness levels of four indicators

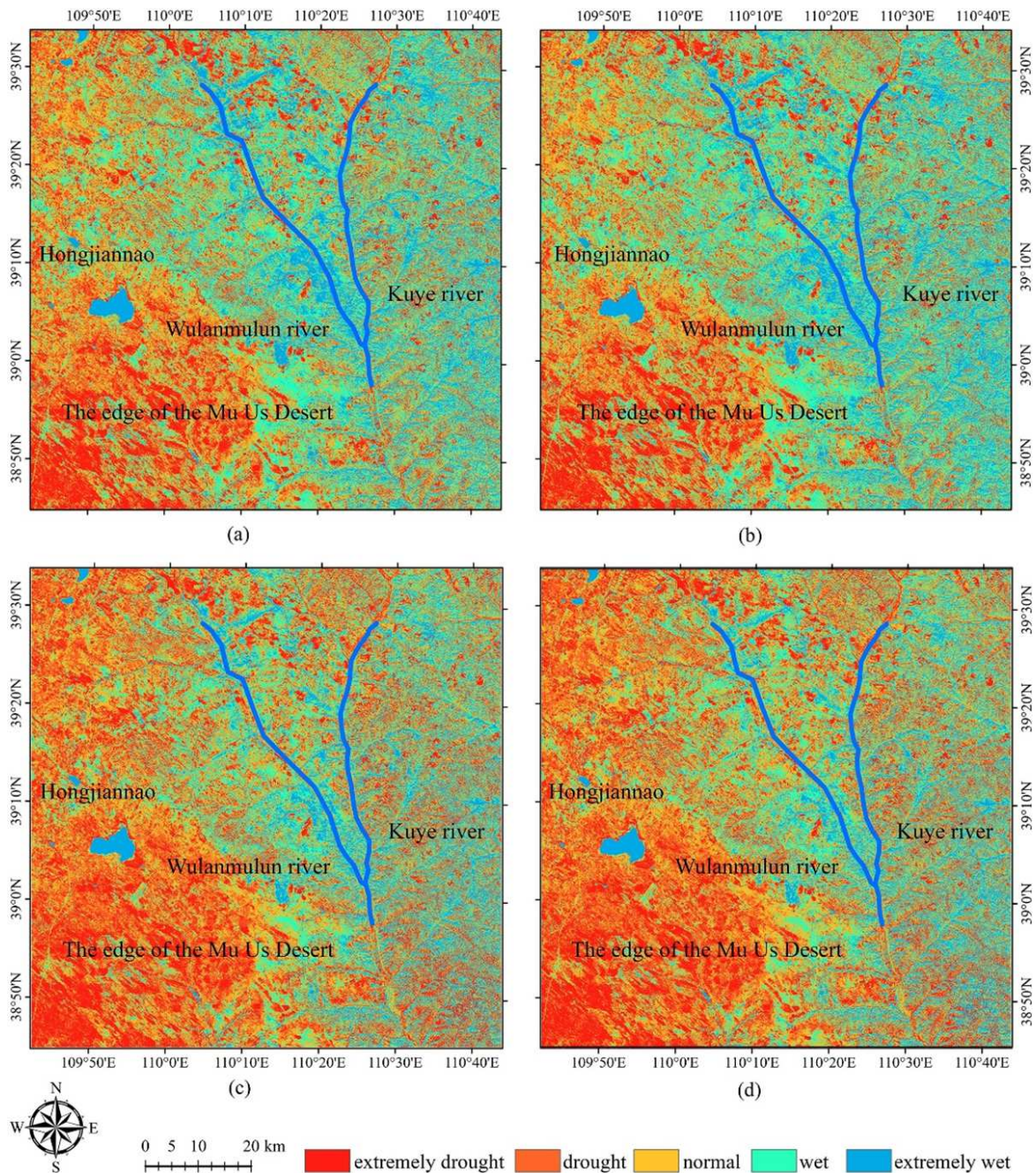
Satellite	Indices	extremely wet	wet	normal	dryness	extremely dryness
GF-1	SMMI	20.38	29.93	24.30	13.30	12.09
	PDI	19.22	29.75	24.68	13.78	12.57
	MPDI	15.26	23.87	26.73	18.86	15.28
	MSMMI	18.97	25.72	25.13	16.40	13.78
Landsat-8	SMMI	15.67	25.74	27.72	17.05	13.82
	PDI	16.54	28.24	26.89	15.48	12.85
	MPDI	11.52	17.77	28.18	24.81	17.72
	MSMMI	12.35	18.56	27.48	23.83	17.78



314

315

**Fig.9.** The soil moisture map of GF-1. (a) SMMI. (b) PDI. (c) MSMMI. (d) MPDI.

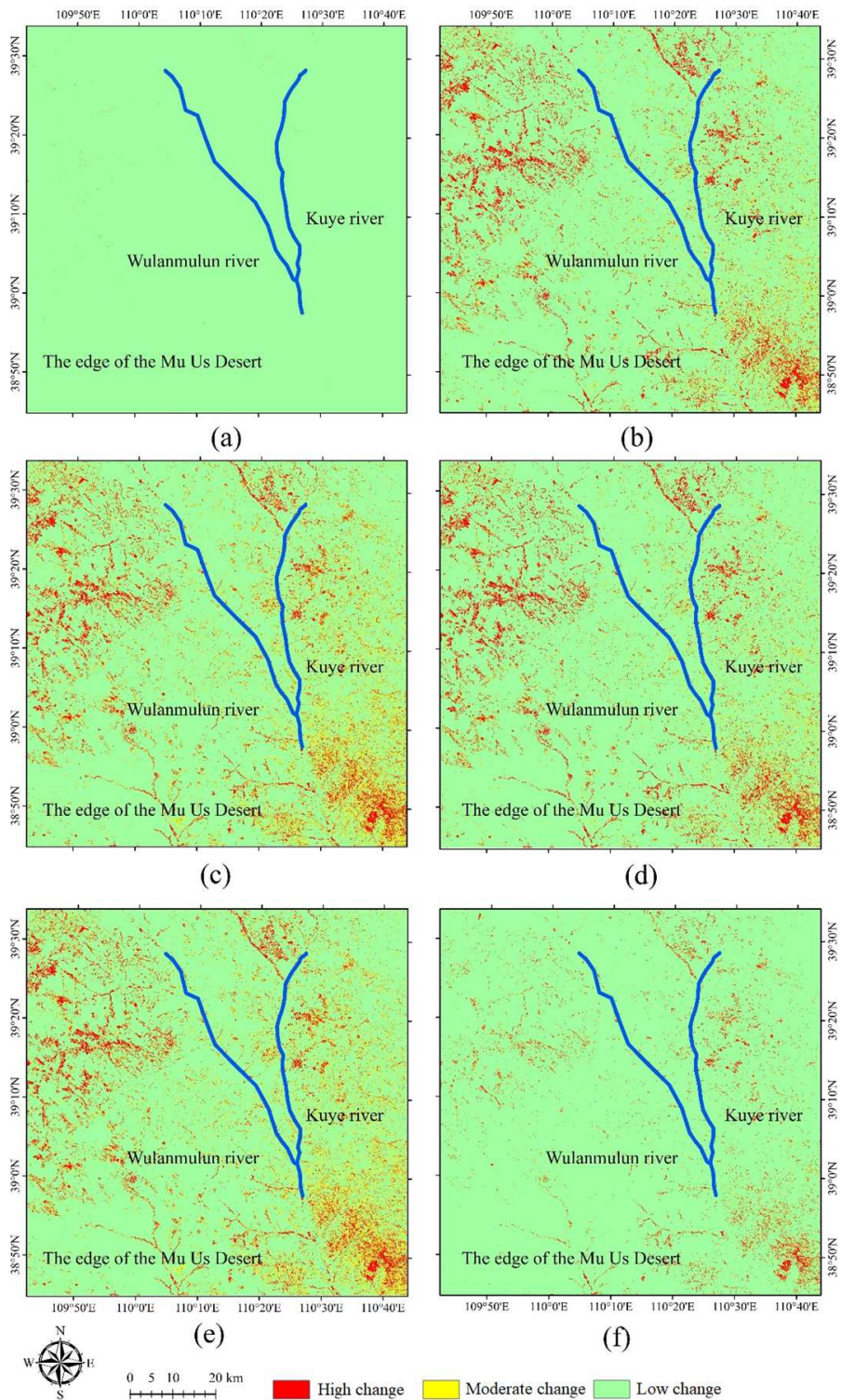


316  
 317 **Fig.10.** The soil moisture map of Landsat-8. (a) SMMI. (b) PDI. (c) MSMMI. (d) MPDI.

318 **3.1.2 Quantitatively measuring the relationship between the four indicators based on GSSIM**

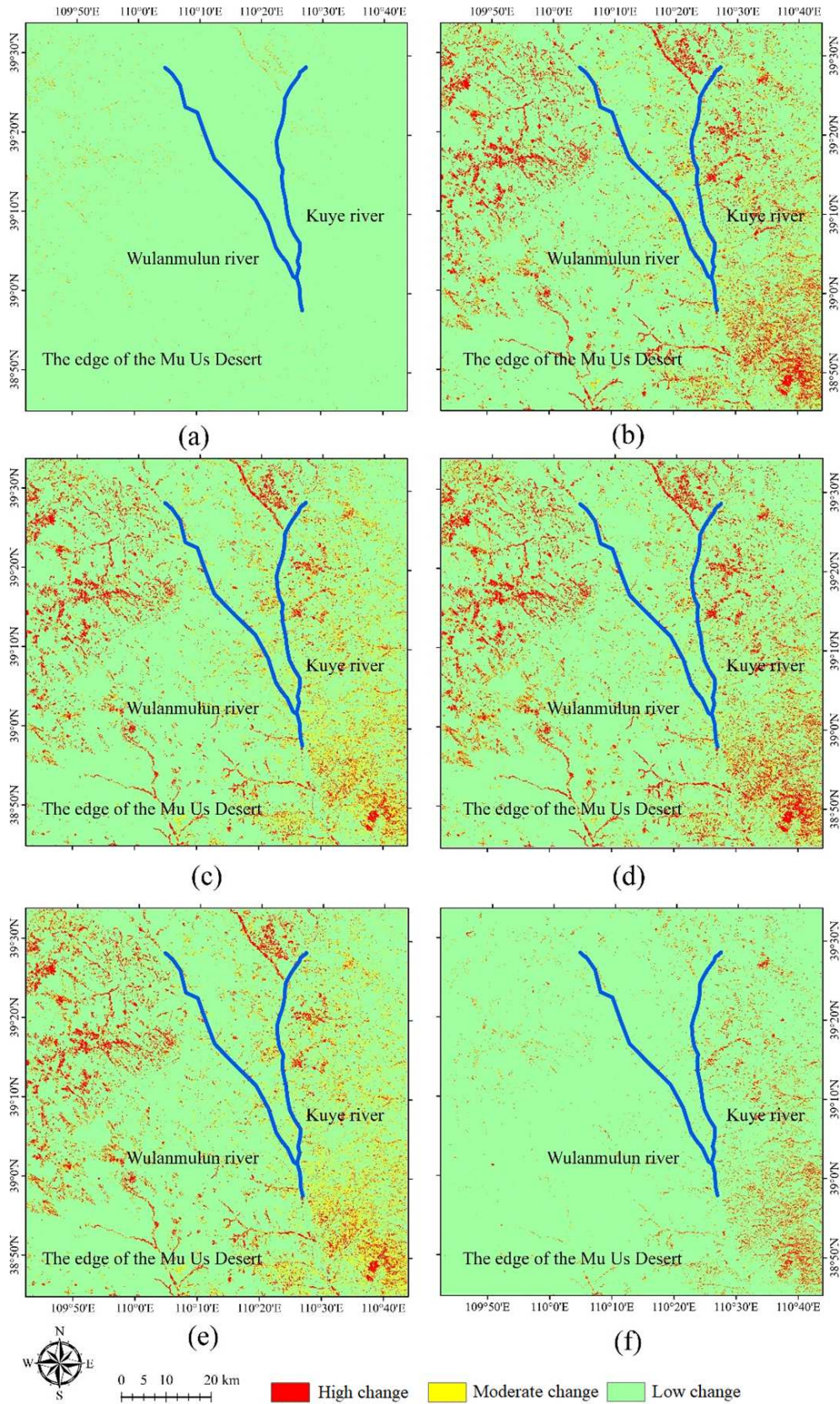
319 Figures 11 and 12 and Table 3 demonstrate that most of the Shendong mining area is in a low change level for  
 320 GSSIM between SMMI and PDI, accounting for 99.89% for GF-1 and 98.89% for L8, which indicates that the  
 321 values of SMMI and PDI are very similar. Figures 11 and 12 and Table 3 also show that most of the Shendong  
 322 mining area is in a low change level for GSSIM between MSMMI and MPDI, accounting for 95.78% for GF-1  
 323 and 94.45% for L8, which also shows that there are almost no differences in the values between MSMMI and  
 324 MPDI. As shown in Table 3, we can see that there are moderate and high change between SMMI and MSMMI,  
 325 SMMI and MPDI, PDI and MSMMI, and PDI and MPDI for GF-1 and L8, ranging from 11.75% to 17.70%, and

326 these changes occur in the west, east and north of the Shendong mining area. This result indicates that there are  
 327 significant differences in the values between SMMI and MSMMI, SMMI and MPDI, PDI and MSMMI, and PDI  
 328 and MPDI in these areas. However, the values of SMMI and MSMMI, SMMI and MPDI, PDI and MSMMI, and  
 329 PDI and MPDI for GF-1 and L8 were very similar, accounting for more than 82% of the study area.



330

331 **Fig.11.** GSSIM map between four indicators of GF-1. (a) GSSIM between SMMI and PDI. (b) GSSIM between  
 332 SMMI and MSMMI. (c) GSSIM between SMMI and MPDI. (d) GSSIM between PDI and MSMMI. (e) GSSIM



334  
 335 **Fig.12.** GSSIM map between four indicators of L8. (a) GSSIM between SMMI and PDI. (b) GSSIM between  
 336 SMMI and MSMMI. (c) GSSIM between SMMI and MPDI. (d) GSSIM between PDI and MSMMI. (e)  
 337 GSSIM between PDI and MPDI. (f) GSSIM between MPDI and MSMMI.  
 338

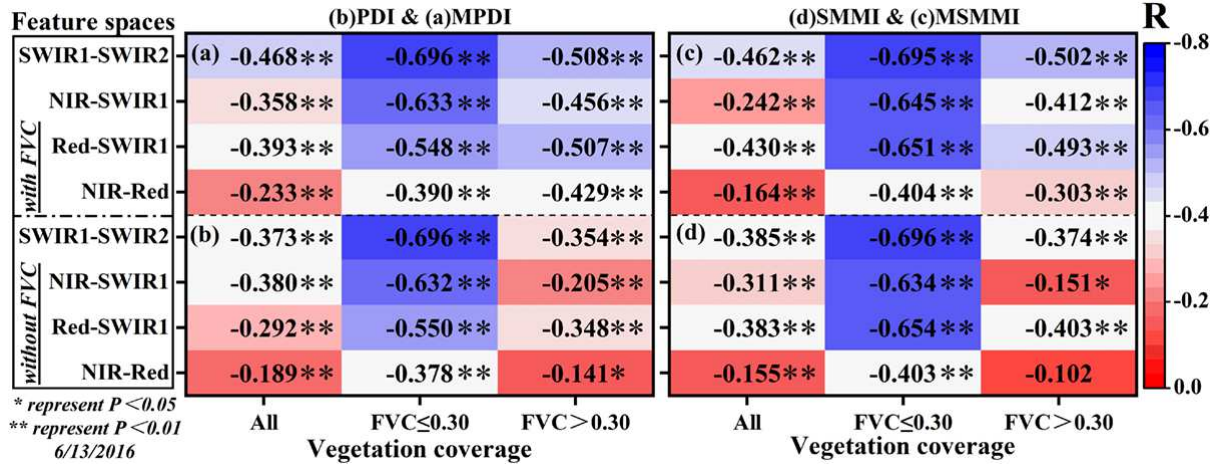
339 **Table 3.** Percentage of GSSIM change levels between four indicators

Satellite	GSSIM	High change	Moderate change	Low change
<b>GF-1</b>	SMMI and PDI	0.01	0.10	99.89
	SMMI and MSMMI	6.55	5.23	88.22
	SMMI and MPDI	6.83	9.89	83.28
	PDI and MPDI	6.59	5.16	88.25
	PDI and MSMMI	6.74	9.92	83.34
	MPDI and MSMMI	2.38	1.84	95.78
<b>L8</b>	SMMI and PDI	0.17	0.94	98.89
	SMMI and MSMMI	9.11	7.41	83.48
	SMMI and MPDI	7.09	9.75	83.16
	PDI and MPDI	9.50	8.03	82.47
	PDI and MSMMI	7.10	10.60	82.30
	MPDI and MSMMI	2.56	2.99	94.45

340 *3.2 Comparison among SMMI, PDI, MSMMI, and MPDI through SMAPVEX16 dataset: Case*  
 341 *II*

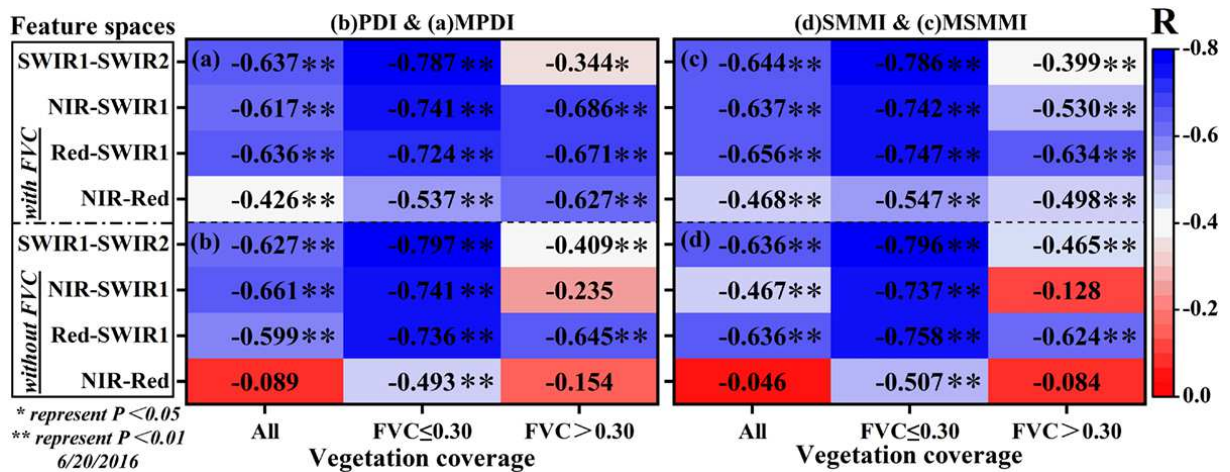
342 Section 3.1 analyzed the performance of four indices for monitoring SM in bare soil areas in arid and semi-arid  
 343 regions. Section 3.2 mainly analyzed the similarities and differences of four indices on monitoring SM in farmland,  
 344 including bare soil and vegetation-covered areas.

345 The soil lines on June 13 and June 20, 2016, in the study area, were extracted from the reflectance image with  
 346  $NDVI < 0.3$ . The soil line of NIR-Red feature space by GF-1 and that by Sentinel-2 was the same. Figures 13 and  
 347 14 show that the indices with the SWIR band have a higher correlation with measured SM. On the whole, the  
 348 correlation between MSMMI and measured SM was significantly higher than that of SMMI. MPDI is higher than  
 349 PDI. The correlation between the indices with FVC and measured SM in bare soil areas was the same as those  
 350 without FVC. However, the correlation between the indices with FVC and measured SM in vegetation-covered  
 351 areas was higher than that without FVC. The indices from NIR-Red space had the lowest correlation with SM,  
 352 whether with or without the participation of FVC. This indicated that indices from SWIR space were more effective  
 353 in monitoring SM than those from NIR-Red space.



354

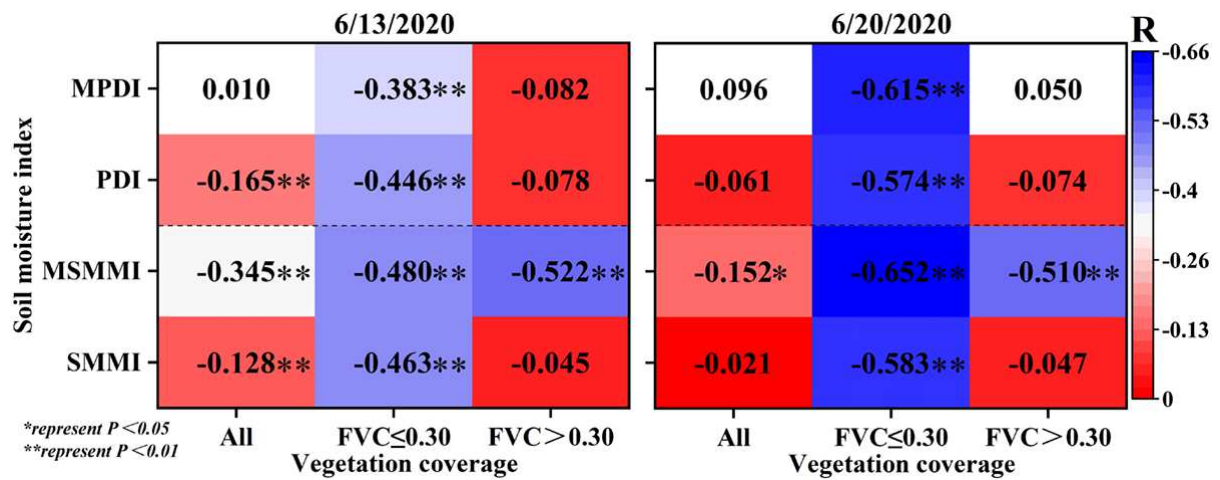
355 **Fig.13.** The relationship between measured SM and soil moisture indices under different land cover types from  
356 Sentinel-2 on June 13, 2016.



357

358 **Fig.14.** The relationship between measured SM and soil moisture indices under different land cover types by  
359 Sentinel-2 on June 20, 2016.

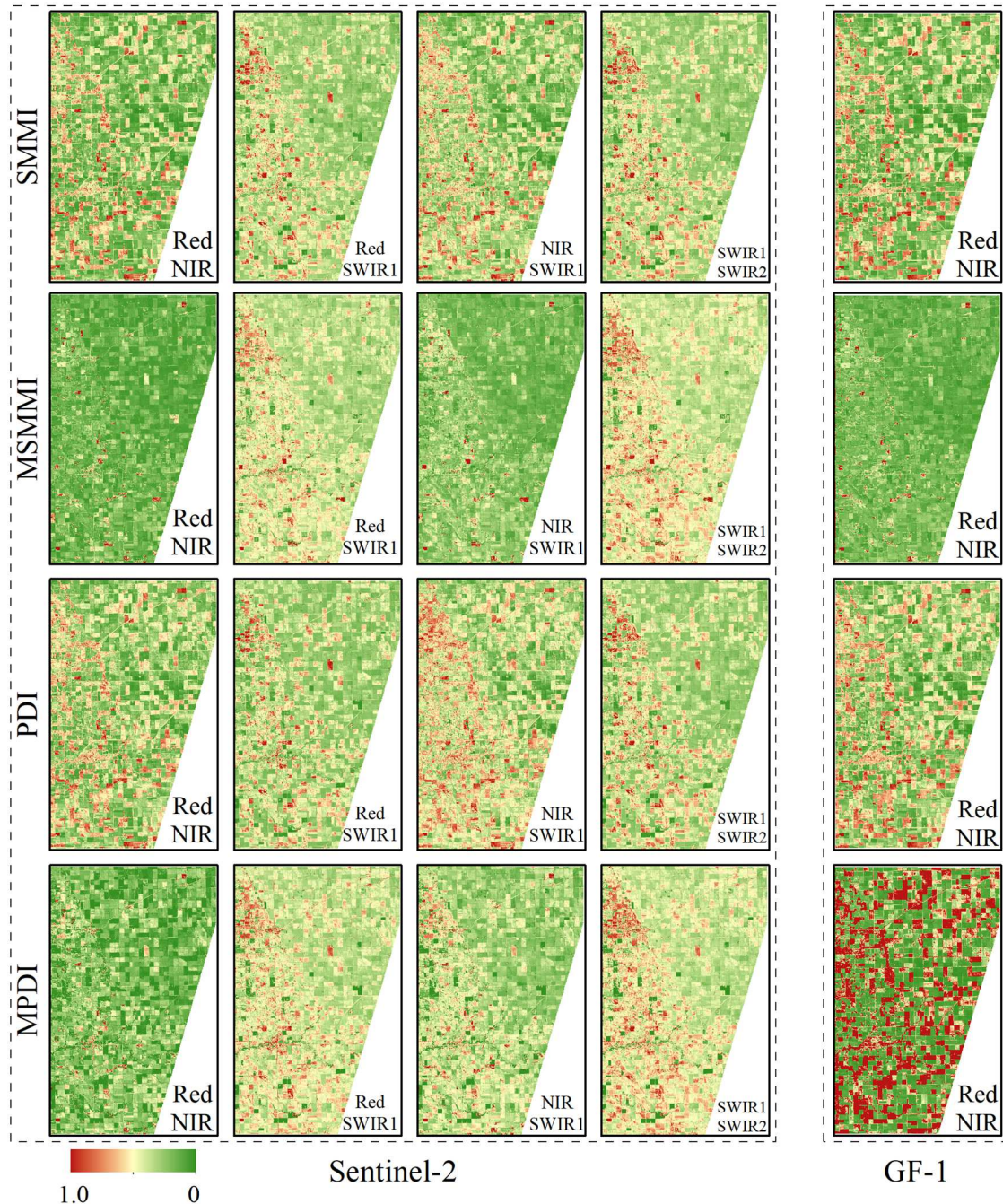
360 Figure 15 showed that the correlation between MSMMI by GF-1 and all measured SM sample points was the  
361 highest on June 13, 2016 ( $R = -0.345$ ,  $P < 0.01$ ). The correlation between MSMMI and bare soil SM and vegetation  
362 areas SM was  $-0.480$  and  $-0.522$ , respectively. The same conclusion was reached on June 20, 2016. However, the  
363 correlation between MSMMI from GF-1 and all measured SM sample points was relatively low ( $R = -0.152$ ,  $P <$   
364  $0.05$ ). The correlations between the other three indices and measured SM in bare soil areas were lower than that  
365 of MSMMI, which were significantly lower in vegetation-covered areas.



366

367 **Fig.15.** The relationship between measured SM and soil moisture indices under different land cover types by GF-  
368 1 on June 13 and June 20, 2016.

369 Figure 16 shows that the spatial distribution of the four indices was consistent. The dry areas were mainly  
370 located in bare soil and part of vegetated areas in the central and western regions, while the wet areas were mainly  
371 located in bare soil and vegetated areas in the eastern regions. However, there were a large number of outliers in  
372 the MPDI acquired from GF-1. This was mainly because the FVC of GF-1 was derived from an empirical formula,  
373 while the FVC of Sentinel-2 was obtained through regression model inversion, which can more accurately  
374 represent the surface coverage of the study area. This further indicated that MPDI was more sensitive to FVC  
375 inversion and MSMMI is more applicable for SM monitoring.

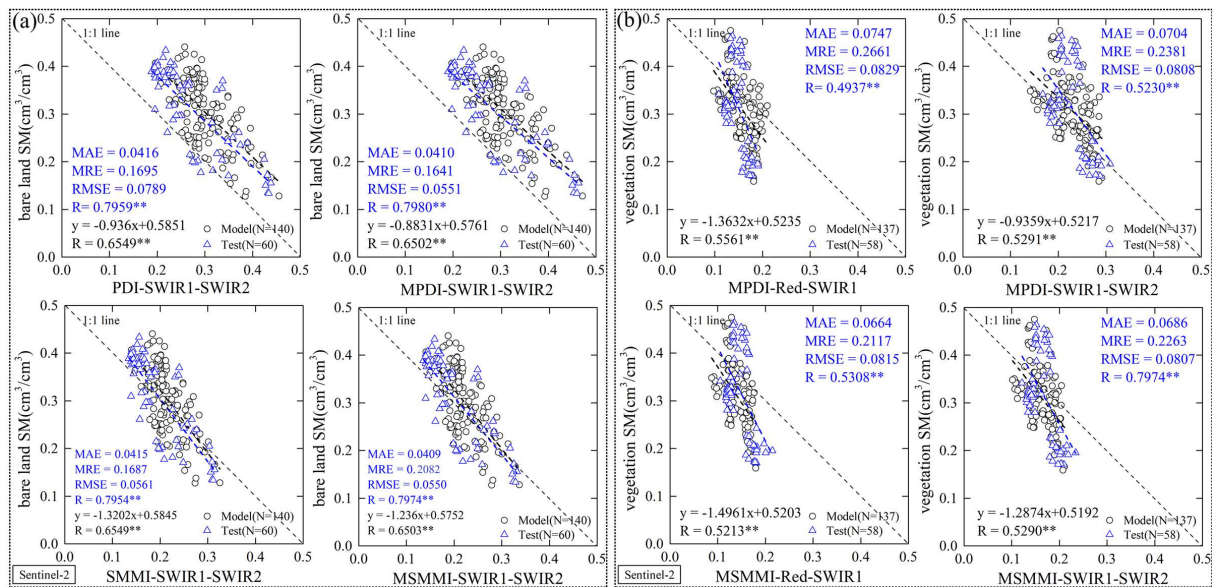


376

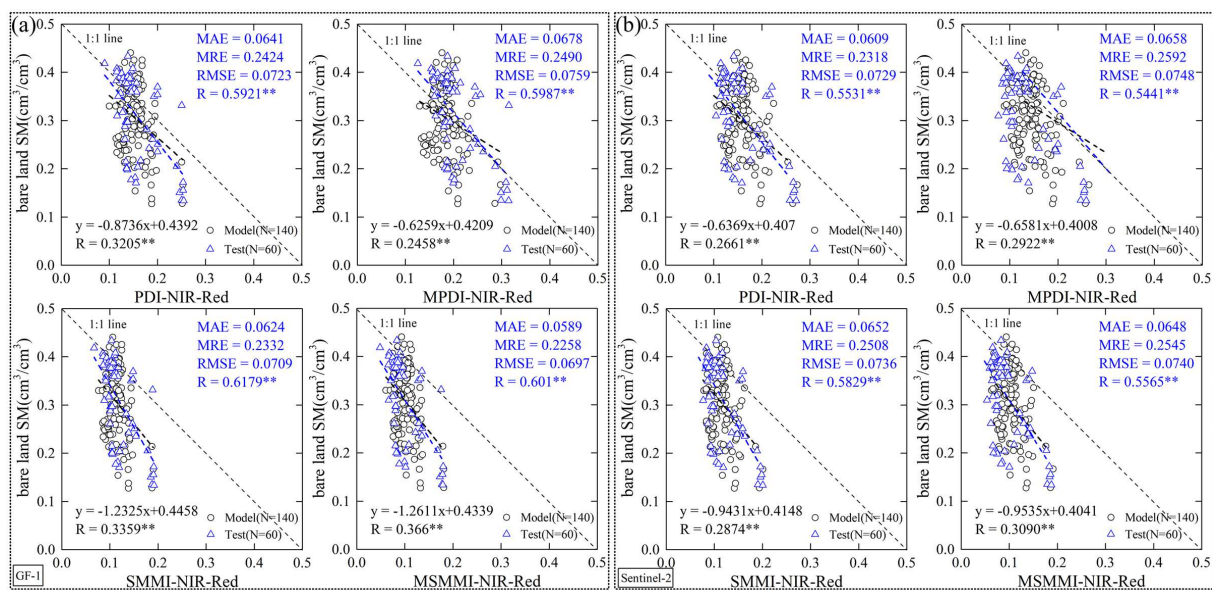
377 **Fig.16.** Spatial distribution of the four indices by Sentinel-2 and GF-1 on June 13, 2016.

378 As shown in Figure 17, the MAE, MRE, and RMSE of PDI from SWIR1-SWIR2 space were  $0.0416 \text{ cm}^3/\text{cm}^3$ ,  
 379  $0.1695$ , and  $0.0789 \text{ cm}^3/\text{cm}^3$ , respectively. The accuracy of MPDI from SWIR1-SWIR2 space were  $0.0410$   
 380  $\text{cm}^3/\text{cm}^3$ ,  $0.1641$ , and  $0.0551 \text{ cm}^3/\text{cm}^3$ , respectively. The accuracy of SMMI from SWIR1-SWIR2 space was  
 381  $0.0415 \text{ cm}^3/\text{cm}^3$ ,  $0.1687$ , and  $0.0561 \text{ cm}^3/\text{cm}^3$ , respectively. The accuracy of MSMMI from SWIR1-SWIR2 space  
 382 are  $0.0409 \text{ cm}^3/\text{cm}^3$ ,  $0.2082$ , and  $0.0550 \text{ cm}^3/\text{cm}^3$ , respectively. This indicated that the estimation accuracy in bare

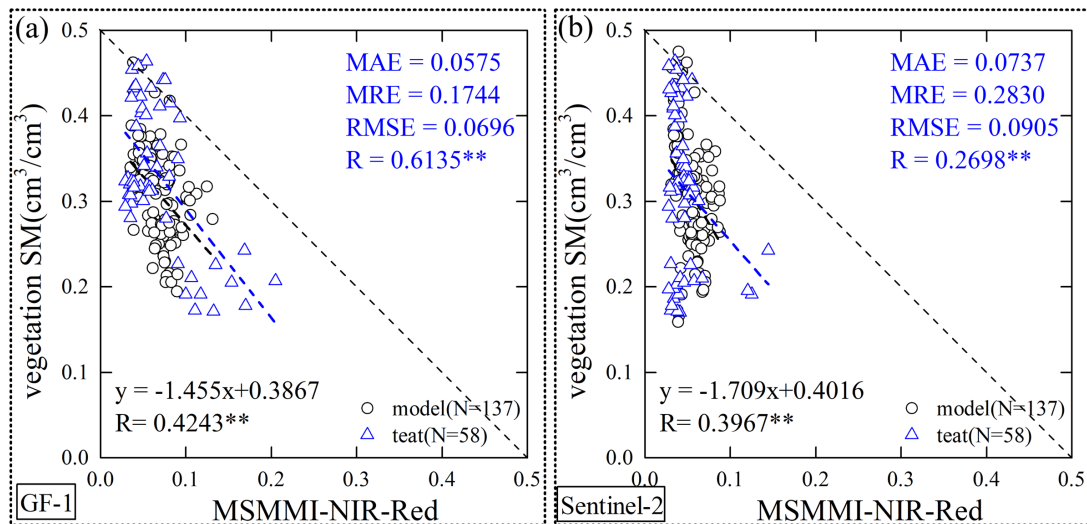
383 soil areas of the four indices from SWIR1-SWIR2 space by Sentinel-2 was similar. Figure 18 shows that the  
 384 estimation accuracy of SM in bare soil areas by GF-1 is slightly better than that by Sentinel-2. The estimation  
 385 accuracy from SWIR1-SWIR2 space was significantly higher than that of NIR-Red space by Sentinel-2. Figure  
 386 19 shows that the estimation accuracy of SM in vegetation-covered areas by MSMMI from NIR-Red space through  
 387 GF-1 is better than that through Sentinel-2, which is lower than that from SWIR1-SWIR2 space of Sentinel-2.



388  
 389 **Fig.17.** (a) The relationship among SMMI, PDI, MSMMI, MPDI, and SM in bare soil areas from SWIR1-SWIR2  
 390 space of Sentinel-2 on June 13, 2016. (b) The relationship among SMMI, PDI, MSMMI, MPDI, and SM in  
 391 vegetation-covered areas from SWIR1-SWIR2 space of Sentinel-2 on June 13, 2016.

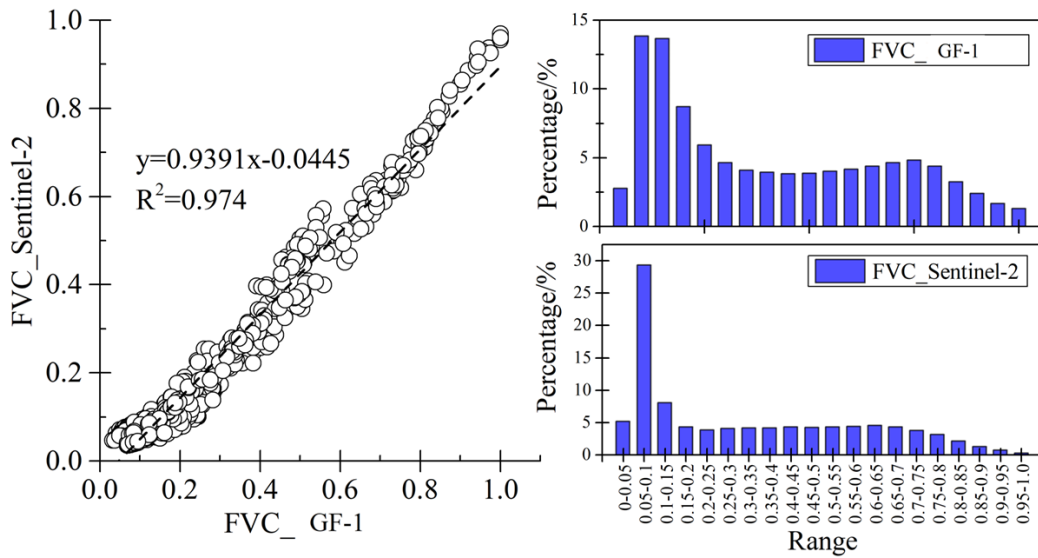


392  
 393 **Fig.18.** The relationship among SMMI, PDI, MSMMI, MPDI, and SM in bare soil areas from NIR-Red space on  
 394 June 13, 2016. (a) GF-1, (b) Sentinel-2



395  
 396 **Fig.19.** The relationship between MSMMI and SM in vegetation-covered areas from NIR-Red space on June 13,  
 397 2016.

398 The differences in SM monitoring between GF-1 and Sentinel-2 were mainly affected by the spatial resolution  
 399 of the image, spectral response function, atmospheric correction method, and vegetation coverage estimation  
 400 method. The Sentinel-2 FVC was extracted by the Biophysical Processor in SNAP software, which combined the  
 401 PROSPECT+SAIL radiation transfer model and artificial neural network to estimate FVC. The GF-1 FVC was  
 402 extracted according to the NDVI threshold of the image and determined by the FVC formula. It can be seen from  
 403 Figure 20, although the correlation between the two FVC results is high, the distribution of the histogram is  
 404 significantly different. The inconsistency of the FVC estimation method may be one of the important reasons for  
 405 the difference between the Sentinel-2 and GF-1 in SM estimation. This may also be the reason why outliers  
 406 appeared in vegetation-covered areas when GF-1 was applied to calculate MPDI. In the future, it will be necessary  
 407 to explore the optimal calculation method of FVC using MPDI and MSMMI to monitor SM in vegetation-covered  
 408 areas.



409  
410 **Fig.20.** Correlation and histogram of two FVC methods on June 13, 2016

411 **4. Discussion**

412 *4.1 Comparison with previous studies*

413 The results of soil moisture estimation in two cases indicated that NIR-Red feature space can reflect the dry and  
 414 wet conditions of bare soil, but cannot effectively monitor the dryness and wetness status in vegetated areas. This  
 415 was consistent with the findings of Ghulam et al. (2007b), PDI was more suitable for monitoring soil moisture in  
 416 bare soil or areas with sparse vegetation. To address the weaknesses of PDI based on the NIR-Red feature space,  
 417 Ghulam et al. (2007c) proposed a new index (Shortwave infrared perpendicular water stress index, SPSI) based  
 418 on the NIR-SWIR feature space, which had the potential in estimating vegetation water content and SM. Fensholt  
 419 et al. (2003) adopted NIR and SWIR bands from MODIS data to establish short-wave infrared water stress index  
 420 (SIWSI) and showed that there was a strong correlation between SIWSI and SM. Ma et al. (2018) applied Sentinel-  
 421 1 dual-polarized SAR data to invert SM in the semi-arid region of China and compared it with the SMMI from  
 422 NIR-SWIR2 space based on Landsat images. The results showed that SMMI from NIR-SWIR2 space could  
 423 effectively reflect the surface dry and wet distribution in a semi-arid area, but there was an overestimation in sandy  
 424 land. Koley et al. (2020) demonstrated that the accuracy of SM derived from the SWIR2 band from Sentinel-2 and  
 425 Landsat-8 was more accurate than the thermal infrared band. It can be found that although the band combinations

426 of these soil moisture indices are slightly different, which is greatly related to the actual surface cover of the study  
 427 area, they all involved SWIR bands. In this study, the correlations between the indices from NIR-Red space and  
 428 SM in agricultural vegetation-covered areas were much lower than that from SWIR1-SWIR2 space. As a strong  
 429 absorptive band of water vapor, SWIR bands can effectively reflect SM in bare soil and vegetated areas (Ghulam  
 430 et al., 2007c; Ma et al., 2018). Besides, the overall accuracy of SM by SMMI was slightly higher than that of PDI,  
 431 mainly because SMMI did not consider the soil line, which was significantly different under the influence of soil  
 432 texture, soil fertility, vegetation cover types, and other factors in the study area. The overall accuracy of SM from  
 433 MSMMI was also higher than that of MPDI.

#### 434 4.2 The relationship between SMMI, PDI, MSMMI, and MPDI

435 Figure 21 shows that the PDI is the leg of the right triangle EFO, whose hypotenuse is SMMI. When point E is  
 436 located in an area with infinite distance, the PDI is equal to SMMI. There is an algebraic relation between PDI and  
 437 SMMI, which can be written as

$$438 \quad SMMI = \sqrt{PDI^2 + (PVI - |OH|)^2} \quad (13)$$

439 with

$$440 \quad PVI = \frac{|R_{NIR} - MR_{Red} - I|}{\sqrt{1 + M^2}} \quad (14)$$

441 where I is the intercept of the soil line BC.

442 In equation 13, the value of  $|OH|$  can be acquired as follows:

443 The line L can be expressed as

$$444 \quad R_{NIR} = -\frac{1}{M} R_{Red} \quad (15)$$

445 The soil line BC can be written as

$$446 \quad R_{NIR} = MR_{Red} + I \quad (16)$$

447 When equations 15 and 16 are combined, point H ( $H_{NIR}, H_{Red}$ ) can be indicated as

448 
$$\begin{cases} H_{\text{NIR}} = -\frac{1}{M} H_{\text{Red}} \\ H_{\text{NIR}} = M H_{\text{Red}} + I \end{cases} \quad (17)$$

449 Thus, the coordinates of point H ( $H_{\text{NIR}}$ ,  $H_{\text{Red}}$ ) can be written as

450 
$$\begin{cases} H_{\text{Red}} = \frac{-MI}{1+M^2} \\ H_{\text{NIR}} = \frac{I}{1+M^2} \end{cases} \quad (18)$$

451 We can obtain the value  $|OH|$  from equation 18, which can be expressed as

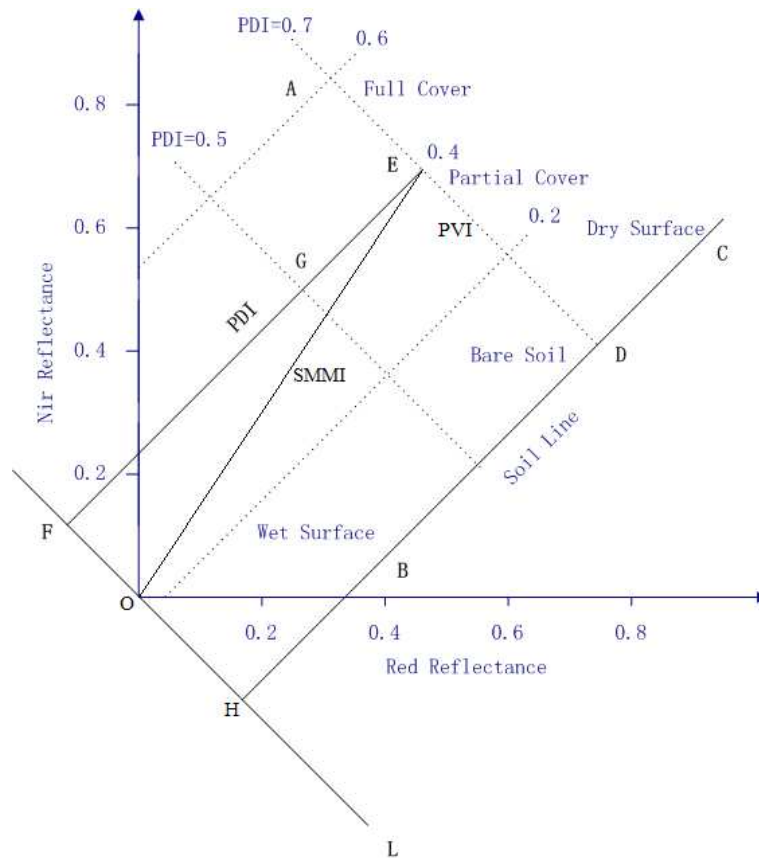
452 
$$|OH| = \frac{I\sqrt{1+M^2}}{1+M^2} \quad (19)$$

453 Therefore, the relationship between the SMMI and PDI can be written as

454 
$$\text{SMMI} = \sqrt{\text{PDI}^2 + \left(\text{PVI} - \frac{I\sqrt{1+M^2}}{1+M^2}\right)^2} \quad (20)$$

455 Equation 20 demonstrates that the SMMI is a combination of the PDI, PVI, the slope (M), and intercept (I). This  
 456 result also explains why most of the part in the GSSIM map between the SMMI and PDI is at a low change level  
 457 and why the SMMI and PDI have a similar ability to monitor soil moisture. However, section 3.1 shows that the  
 458 SMMI is better in retrieving soil moisture than the PDI, which was better than the MSMMI and MPDI in the  
 459 Shendong mining area. Moreover, the PDI and MPDI depend on a fixed soil line, which varied with soil type and  
 460 fertilization, causing uncertainty in the dryness or soil moisture evaluation (Ghulam et al. 2007a; Qin et al. 2008;  
 461 Yao et al. 2011). Section 3.2 shows that the MPDI, MSMMI, and SMMI are equivalent in retrieving soil moisture  
 462 and better than PDI in bare soil of agricultural areas. MSMMI is better than SMMI, PDI, and MPDI in vegetation-  
 463 covered areas of agricultural areas. The SMMI relies on only the reflectance of two bands, not on the fixed soil  
 464 lines (Liu et al. 2013; Liu et al. 2017). The SMMI involves fewer parameters than the PDI, and the calculation  
 465 process is simpler than that for the PDI, which is more suitable for soil moisture monitoring in bare soil areas or  
 466 areas with low vegetation coverage. The monitoring effect of SMMI and MSMMI is the same, and the latter

467 considering vegetation coverage is more suitable for monitoring soil moisture in vegetation areas.



468  
469 **Fig.21.** Relationship between PDI and SMMI.

470 **5. Conclusions**

471 There are two types of dryness/soil moisture monitoring indices based on NIR-red space, i.e., PDI, MPDI, and  
472 SMMI, MSMMI. PDI and MPDI depend on a soil line, involving in the reflectance of NIR and red bands, and the  
473 slope M of the soil line, which varies with soil type and fertilization. SMMI and MSMMI refer to only the  
474 reflectance of NIR and red bands, which do not rely on the soil line. In this study, the potential and differences of  
475 the SMMI and MSMMI were compared with the PDI and MPDI from GF-1, Landsat-8, and Sentinel-2. Although  
476 they were significantly correlated with the field-measured soil moisture (FSM), the R between the estimated soil  
477 moisture from SMMI and FSM was higher than that from PDI, which was higher than that from the MSMMI and  
478 MPDI in the Shendong mining area because of the low vegetation coverage. GSSIM was employed to  
479 quantitatively assess the performances of these four indicators. The results showed that the SMMI, which is the

480 hypotenuse of the right triangle EFO, had the same potential as PDI, which is the leg of the right triangle EFO, in  
481 monitoring soil moisture. Moreover, MSMMI and MPDI were also very similar. In the aspect of monitoring soil  
482 moisture in the bare soil area of farmland in Canada, the performance of the four indexes was the same. However,  
483 in terms of soil moisture in vegetated areas, MSMMI and MPDI introduced by vegetation coverage and short-  
484 wave infrared bands were superior to SMMI and PDI. This indicated that SMMI, which was simple, effective, and  
485 operational, was more suitable than the PDI in retrieving SM in bare soil areas or areas with low vegetation  
486 coverage. MSMMI with the introduction of vegetation coverage and the short-wave infrared band was more  
487 suitable for monitoring SM in vegetation-covered areas. The comparison between GF-1 WFV sensors and Landsat-  
488 8 OLI showed that GF-1 with 16 m resolution had higher accuracy than Landsat-8 in soil moisture assessment.  
489 The Sentinel-1 MSI and GF-1 WFV had similar accuracy in monitoring SM in bare soil. However, GF-1 cannot  
490 monitor SM in vegetation-covered areas due to the lack of short-wave infrared bands.

491 **Authors' contributions** methodology and writing, H. Y., data curation, Y. L., modified the whole paper, H. Y.,  
492 Y. L., and J. X. Q., revised the whole paper, Y.L., and H.Y.

493 **Funding** This work was jointly supported by the Natural Science Basic Research Program of Shaanxi (2020JM-  
494 514), Research on Ecological Restoration and Protection of Coal Base in Arid Eco-fragile Region  
495 (GJNY2030XDXM-19-03.2), the project of Shaanxi Coal and Chemical Industry Group (2018SMHKJ-A-J-03),  
496 Xi'an University of Science and Technology (2019YQ3-04).

497 **Data availability** Extra data is available by emailing 13720559861@163.com on reasonable request.

498 **Compliance with ethical standards**

499 **Competing interests** The authors declare that they have no competing interests.

500 **Ethics approval and consent to participate** Not applicable.

501 **Consent to publish** Not applicable.

## 502 **References**

- 503 Alizadeh, M. R., & Nikoo, M. R. 2018. A fusion-based methodology for meteorological dryness estimation using remote  
504 sensing data. *Remote Sensing of Environment*, 211, 229-247.
- 505 Amani, M., Salehi, B., Mahdavi, S., Masjedi, A., & Dehnavi, S. 2017. Temperature-vegetation-soil moisture dryness index  
506 (TVMDI). *Remote Sensing of Environment*, 197, 1-14.
- 507 Chen N.C., Li, J.Z., Zhang, X. 2015. Quantitative evaluation of observation capability of GF-1 wide field of view sensors for  
508 soil moisture inversion. *Journal of Applied Remote Sensing*, 9(1):199-203.
- 509 Chen, N.C., He, Y.Q., & Zhang, X. 2017. NIR-red spectra-based disaggregation of SMAP soil moisture to 250 m resolution  
510 based on smapex-4/5 in southeastern Australia. *Remote Sensing*, 9(1), 51.
- 511 Dong, T., Meng, L.K., Zhang, W. 2015. Analysis of the application of MODIS shortwave infrared water stress index in  
512 monitoring agricultural dryness. *Journal of Remote Sensing*, 2, 319-327.

513 Dutta, D., Kundu, A., Patel, N.R., Saha, S.K. & Siddiqui, A.R. 2015. Assessment of agricultural dryness in Rajasthan (India)  
514 using remote sensing derived vegetation condition index (VCI) and standardized precipitation index (SPI). *The Egyptian*  
515 *Journal of Remote Sensing and Space Science*, 18(1), 53-63.

516 Entekhabi D, Njoku E G, O'Neill P E, et al. The soil moisture active passive (SMAP) mission[J]. *Proceedings of the IEEE*,  
517 2010, 98(5): 704-716.

518 Fensholt R, Sandholt I. 2003. Derivation of a shortwave infrared water stress index from MODIS near- and shortwave infrared  
519 data in a semiarid environment[J]. *Remote Sensing of Environment*, 87(1): 111-121.

520 Ghulam, A., Qin, Q.M., & Zhan, Z. M. 2007a. Designing of the perpendicular dryness index. *Environmental Geology*, 52(6),  
521 1045-1052.

522 Ghulam, A., Qin, Q., Teyip, T., & Li, Z. L. 2007b. Modified perpendicular dryness index (MPDI): a real-time dryness  
523 monitoring method. *ISPRS Journal of Photogrammetry and Remote Sensing*, 62(2), 150-164.

524 Ghulam A, Li Z L, Qin Q M, et al. 2007c. A method for canopy water content estimation for highly vegetated surfaces-  
525 shortwave infrared perpendicular water stress index[J]. *Science in China Series D: Earth Sciences*, 50(9): 1359-1368.

526 Kang, J., Jin, R., Li, X., Ma, C., Qin, J., & Zhang, Y. 2017. High spatio-temporal resolution mapping of soil moisture by  
527 integrating wireless sensor network observations and MODIS apparent thermal inertia in the Babao River Basin, China.  
528 *Remote Sensing of Environment*, 191, 232-245.

529 Kogan, F.N. 1995a. Dryness of the late 1980s in the United States as derived from NPAA polar-orbiting satellite data. *Bulletin*  
530 *of the American Meteorological Society*, 76(5), 655-668.

531 Kogan, F.N. 1995b. Application of vegetation index and brightness temperature for dryness detection. *Advances in Space*  
532 *Research*, 15, 91-100.

533 Koley S, Jeganathan C. 2020. Estimation and evaluation of high spatial resolution surface soil moisture using multi-sensor  
534 multi-resolution approach[J]. *Geoderma*, 378: 114618.

535 Li, Z., Tan, D., 2013. The second modified perpendicular dryness index (MPDI1): a combined dryness monitoring method with  
536 soil moisture and vegetation index. *Journal of the Indian Society of Remote Sensing*, 41 (4), 873-881.

537 Liu, Y., Wu, L.X., & Yue, H. 2015. Biparabolic NDVI-Ts space and soil moisture remote sensing in an arid and semi arid area.  
538 *Canadian Journal of Remote Sensing*, 41(3), 159-169.

539 Liu, Y., & Yue, H. 2018. The temperature vegetation dryness index (TVDI) based on bi-parabolic NDVI-Ts space and gradient-  
540 based structural similarity (GSSIM) for long-term dryness assessment across Shaanxi province, China (2000-2016).  
541 *Remote Sensing*, 10(6), 959.

542 Liu, Y., Wu, L. X., & Ma, B.D. 2013. Remote sensing monitoring of soil Moisture on the basis of TM/ETM + spectral space.  
543 *Journal of China University of Mining & Technology*, 42, 296-301. (In Chinese)

544 Liu, Y., & Yue, H., Wang, H.R., Zhang, W. 2017. Comparison of SMMI, PDI and its applications in Shendong mining area.  
545 *IOP Conference Series: Earth and Environmental Science*, 57(1), 012025.

546 Price, J. C. 1985. On the analysis of thermal infrared imagery: the limited utility of apparent thermal inertia. *Remote Sensing*  
547 *of Environment*, 18(1):59-73.

548 McNairn H, Gottfried K, and Powers J. Powers. 2018. SMAPVEX16 Manitoba Probe-Based In Situ Soil Moisture Data,  
549 Version 1. Boulder, Colorado USA. NASA National Snow and Ice Data Center Distributed Active Archive Center. doi:  
550 <https://doi.org/10.5067/IUIH8BGW6GDM>.

551 Rao, M., Silber-Coats, Z., Powers, S., Fox Iii, L., & Ghulam, A. 2017. Mapping dryness-impacted vegetation stress in California  
552 using remote sensing. *GIScience & Remote Sensing*, 54(2), 185-201.

553 Rouse, J., Jr.; Haas, R.H.; Schell, J.A.; Deering, D.W. 1974. Monitoring vegetation systems in the Great Plains with ERTS.  
554 *NASA Special Publication*, 351, 309.

555 Qin, Q.M., Ghulam, A., Zhu, L., Wang, L., Li, J., & Nan, P. 2008. Evaluation of MODIS derived perpendicular dryness index  
556 for estimation of surface dryness over northwestern china. *International Journal of Remote Sensing*, 29(7), 1983-1995.

557 Sandholt, I., Andersen, J., & Rasmussen, K. 2002. A simple interpretation of the surface temperature/vegetation index space  
558 for assessment of soil moisture status. *Remote Sensing of Environment*, 79(2), 213-224.

559 Sawada, Y. 2018. Quantifying dryness propagation from soil moisture to vegetation dynamics using a newly developed  
560 ecohydrological land reanalysis. *Remote Sensing*, 10, 1197.

561 Shahabfar, A., Ghulam, A., & Eitzinger, J. 2012. Dryness monitoring in Iran using the perpendicular dryness indices.  
562 *International Journal of Applied Earth Observations & Geoinformation*, 18(1), 119-127.

563 Shahabfar, A. & Eitzinger, J. 2011. Agricultural dryness monitoring in semi-arid and arid areas using MODIS data. *Journal of*  
564 *Agricultural Science*, 149(4):403-414.

565 Shahabfar, A., Ghulam, A., & Conrad, C. 2014. Understanding hydrological repartitioning and shifts in dryness regimes in  
566 central and south-west Asia using MODIS derived perpendicular dryness index and TRMM data. *IEEE Journal of Selected*  
567 *Topics in Applied Earth Observations & Remote Sensing*, 7(3):983-993.

568 Singh, R. P., Roy, S., & Kogan, F. 2003. Vegetation and temperature condition indices from NOAA AVHRR data for dryness  
569 monitoring over India. *International Journal of Remote Sensing*, 24(22), 4393-4402.

570 Yao, Y.J., Qin, Q.M., Zhao, S.H., Yuan, W.L. 2011. Retrieval of soil moisture based on MODIS shortwave infrared spectral  
571 feature. *Journal of Infrared and Millimeter Waves*, 30(1), 9-15. (In Chinese)

572 Zhan, Z. M., Qin, Q. M., Ghulam, A., & Wang, D. D. 2007. NIR-red spectral space based new method for soil moisture  
573 monitoring. *Science China Earth Sciences*, 50(2), 283-289.

574 Zhang, J.Y., Zhang, Q.L., Bao, A.M., Wang, Y.J. 2019. A new remote sensing dryness index based on the near-infrared and red  
575 spectral space. *Remote sensing*, 11(4), 456.

576 Zhang, L., Jiao, W., Zhang, H., Huang, C., & Tong, Q. 2017a. Studying dryness phenomena in the Continental United States  
577 in 2011 and 2012 using various dryness indices. *Remote Sensing of Environment*, 190, 96-106.

578 Zhang, X., Chen, N. 2016. Reconstruction of GF-1 soil moisture observation based on satellite and in situ sensor collaboration  
579 under full cloud contamination. *IEEE Transactions on Geoscience & Remote Sensing*, 54(9):5185-5202.

580 Zormand, S., Jafari, R., & Koupaei, S. S. 2017. Assessment of PDI, MPDI and TVSI dryness indices derived from MODIS  
581 Aqua/Terra level 1B data in natural lands. *Natural Hazards*, 86(2), 757-777.

# Figures

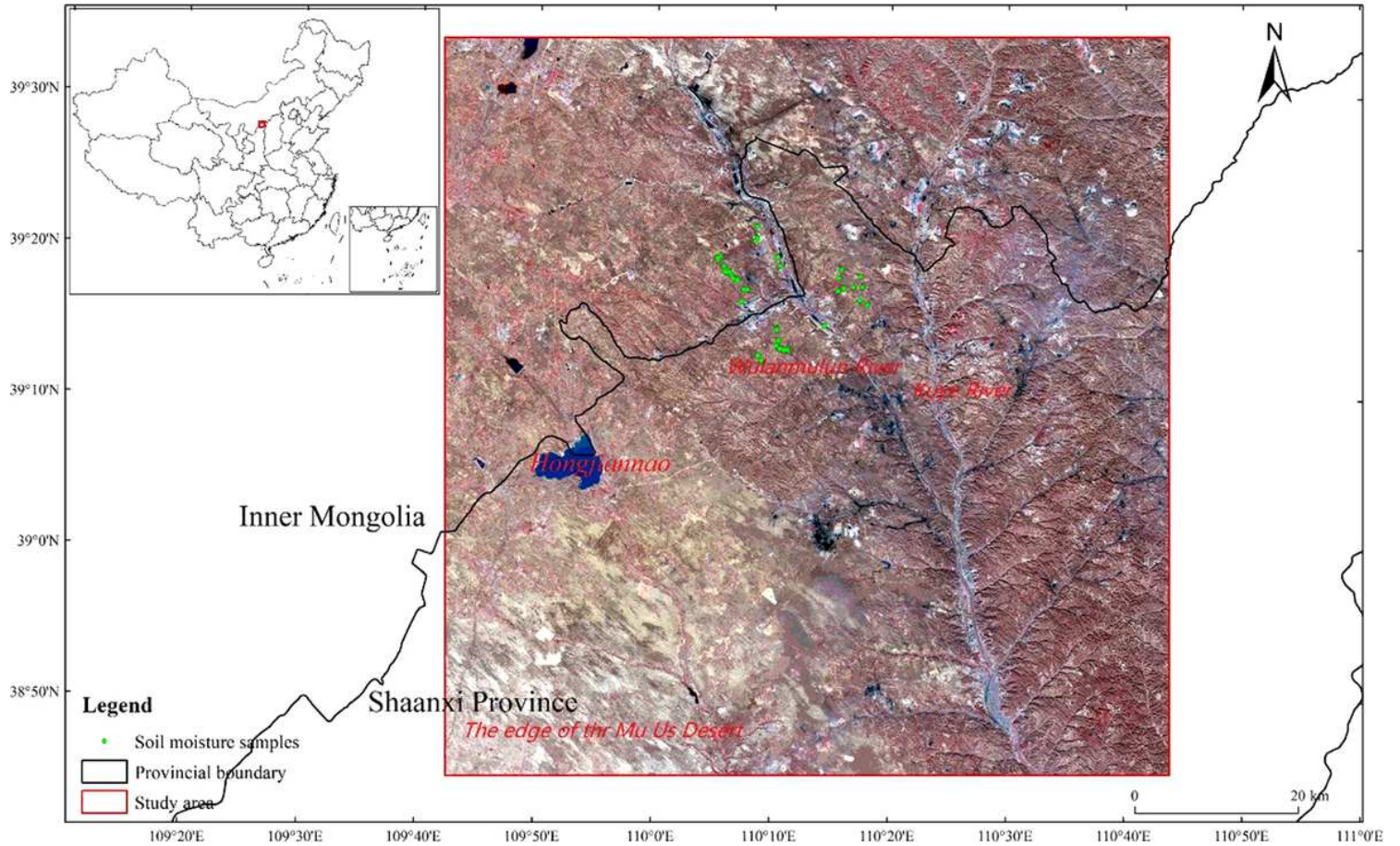


**Figure 1**

Map of Shendong mining area in China. Note: The designations employed and the presentation of the material on this map do not imply the expression of any opinion whatsoever on the part of Research Square concerning the legal status of any country, territory, city or area or of its authorities, or concerning the delimitation of its frontiers or boundaries. This map has been provided by the authors.

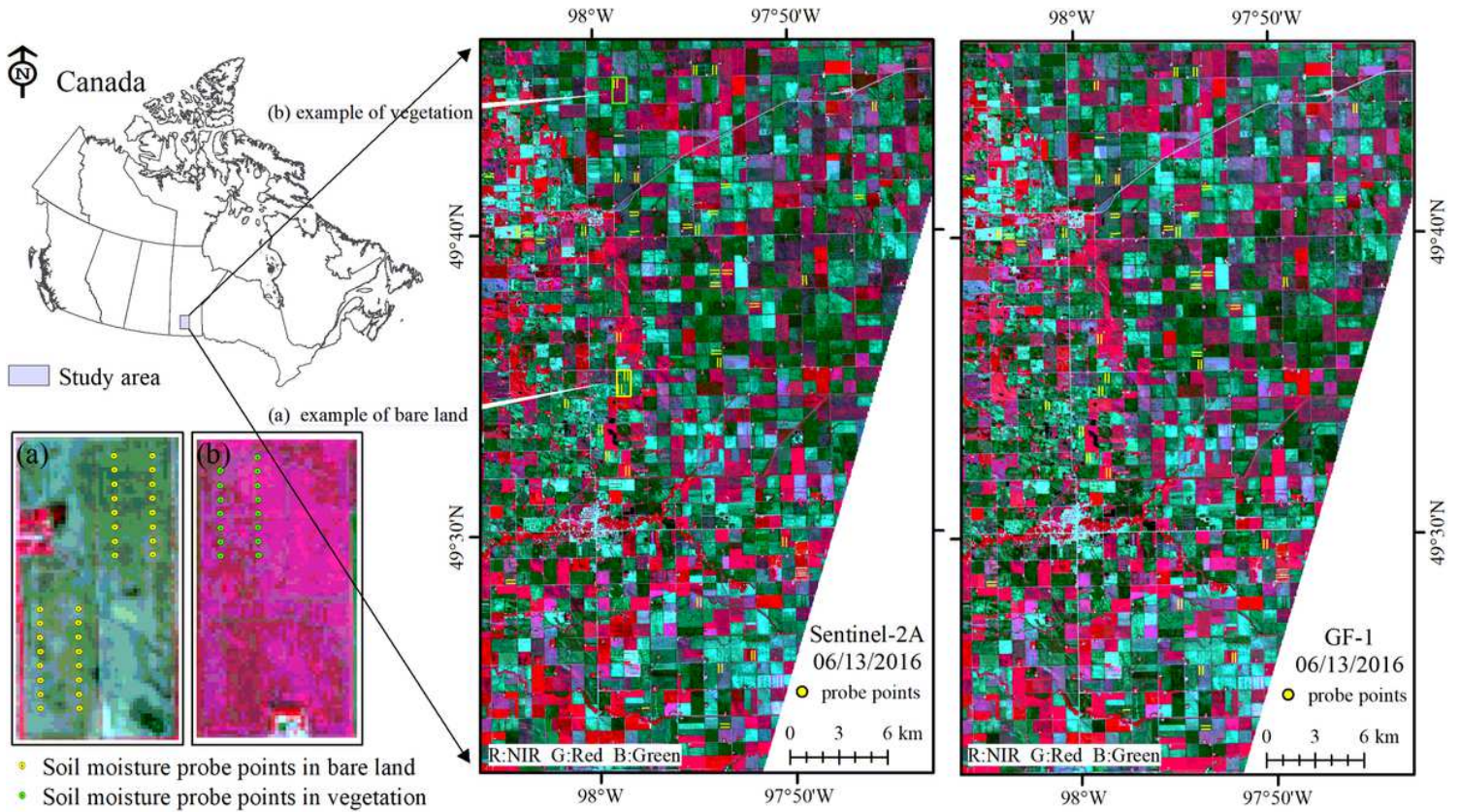


**Figure 2**

The geographic location of the SMAPVEX16 dataset in Canada. Note: The designations employed and the presentation of the material on this map do not imply the expression of any opinion whatsoever on the part of Research Square concerning the legal status of any country, territory, city or area or of its authorities, or concerning the delimitation of its frontiers or boundaries. This map has been provided by the authors.

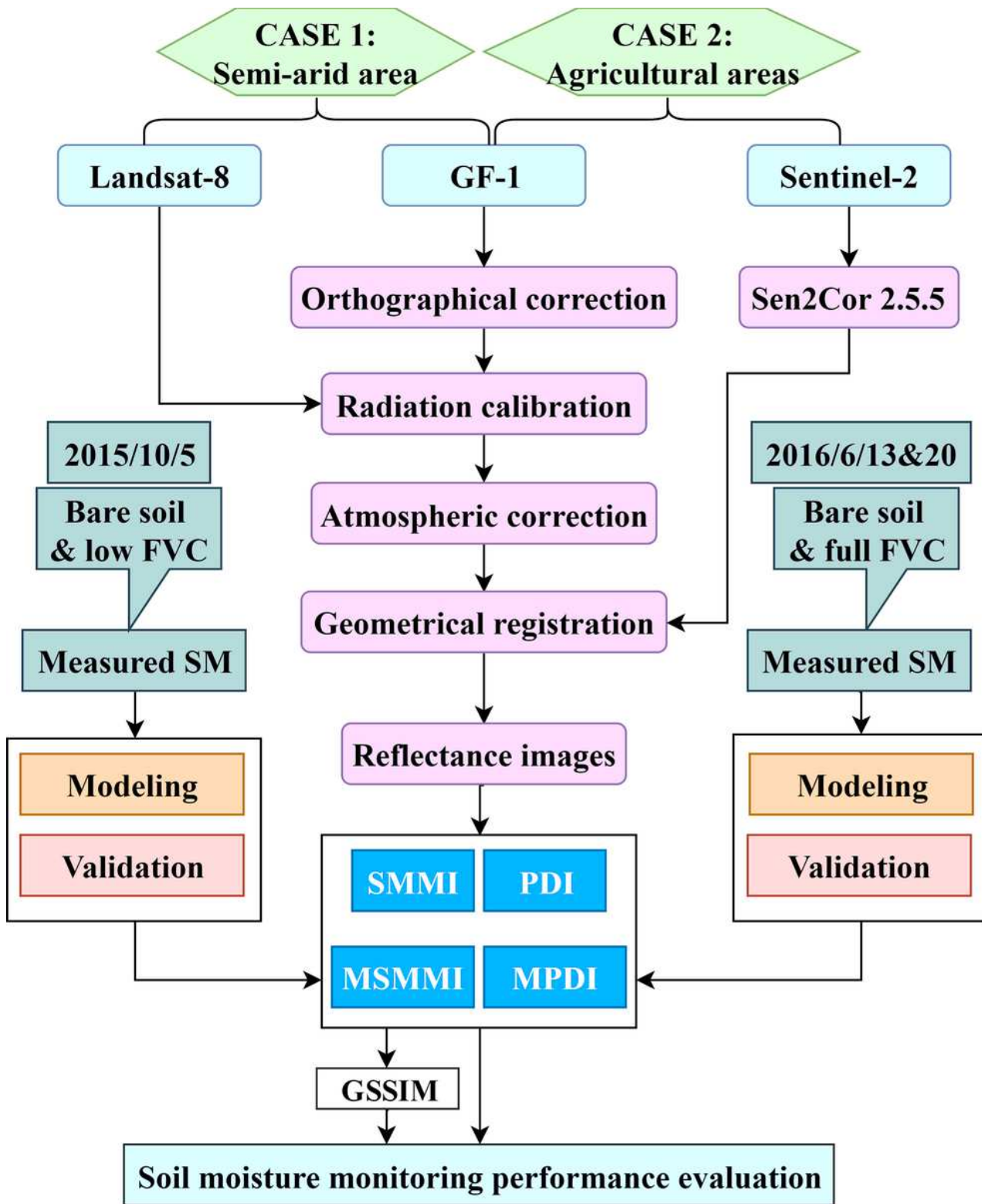
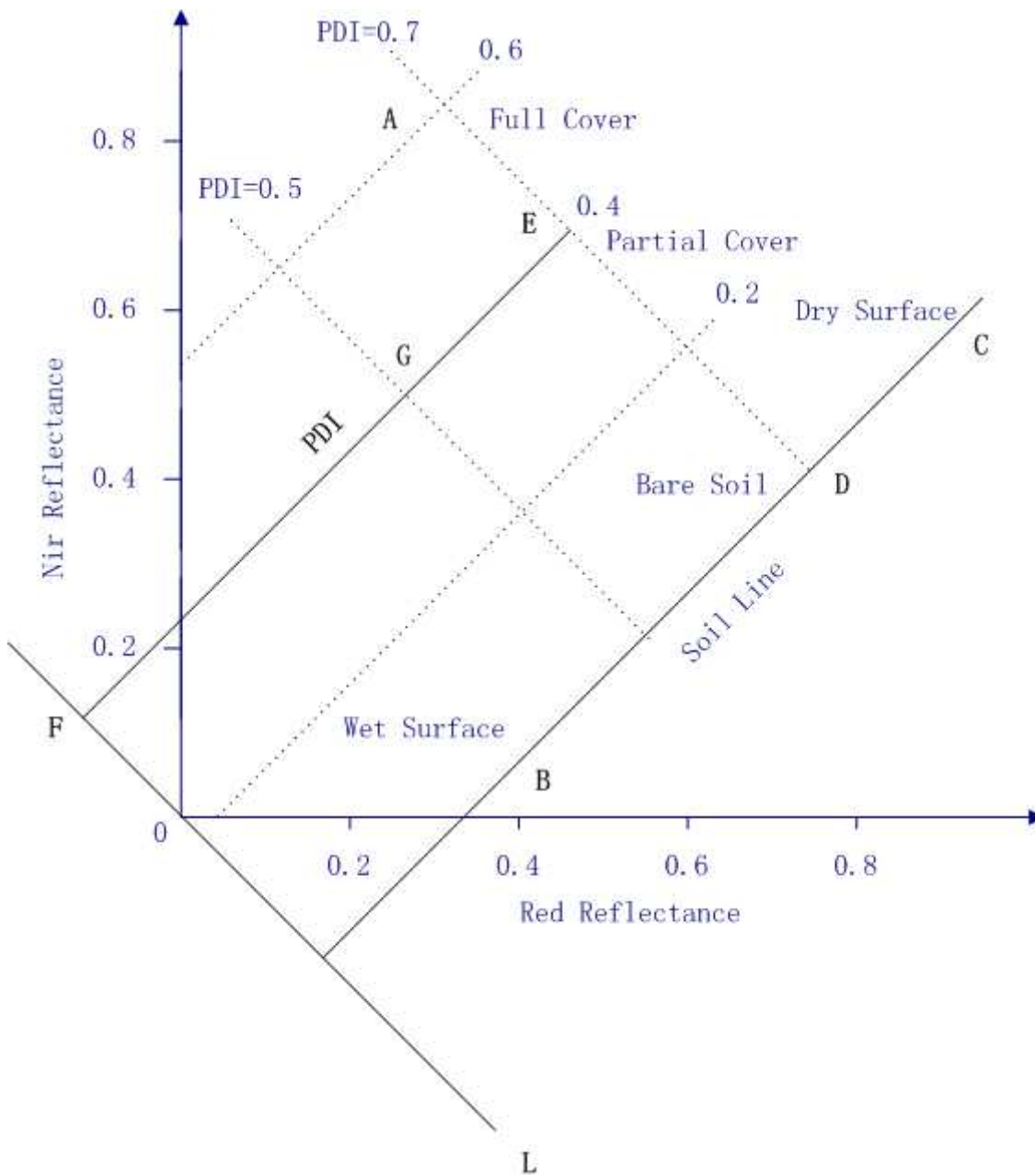


Figure 3

Technical process



**Figure 4**

Sketch map of PDI

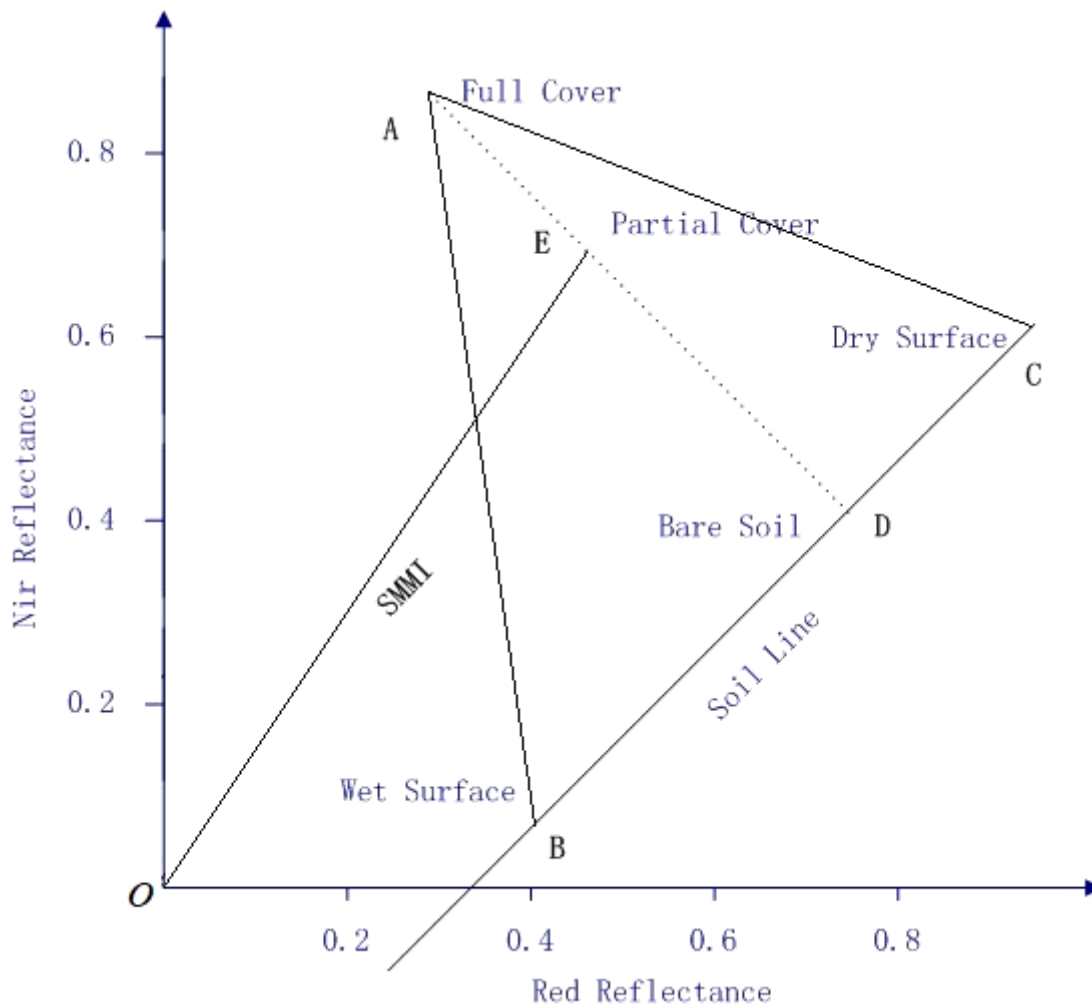


Figure 5

Sketch map of SMMI

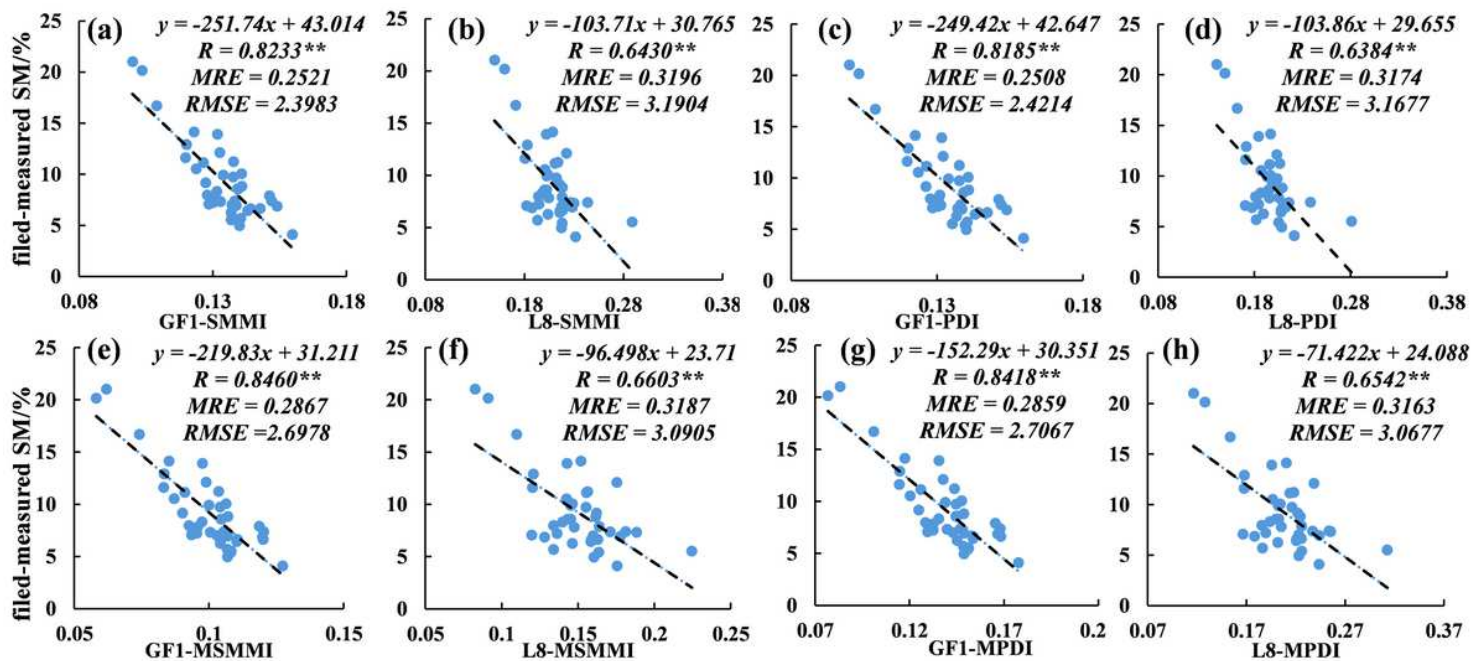


Figure 6

Relationship between four indicators and FSM in 0-5cm depth. (a) GF1-SMMI and FSM. (b) L8-SMMI and FSM (c) GF1-PDI and FSM. (d) L8-PDI and FSM. (e) GF1-MSMMI and FSM. (f) L8-MSMMI and FSM. (g) GF1-MPDI and FSM. (h) L8-MPDI and FSM.

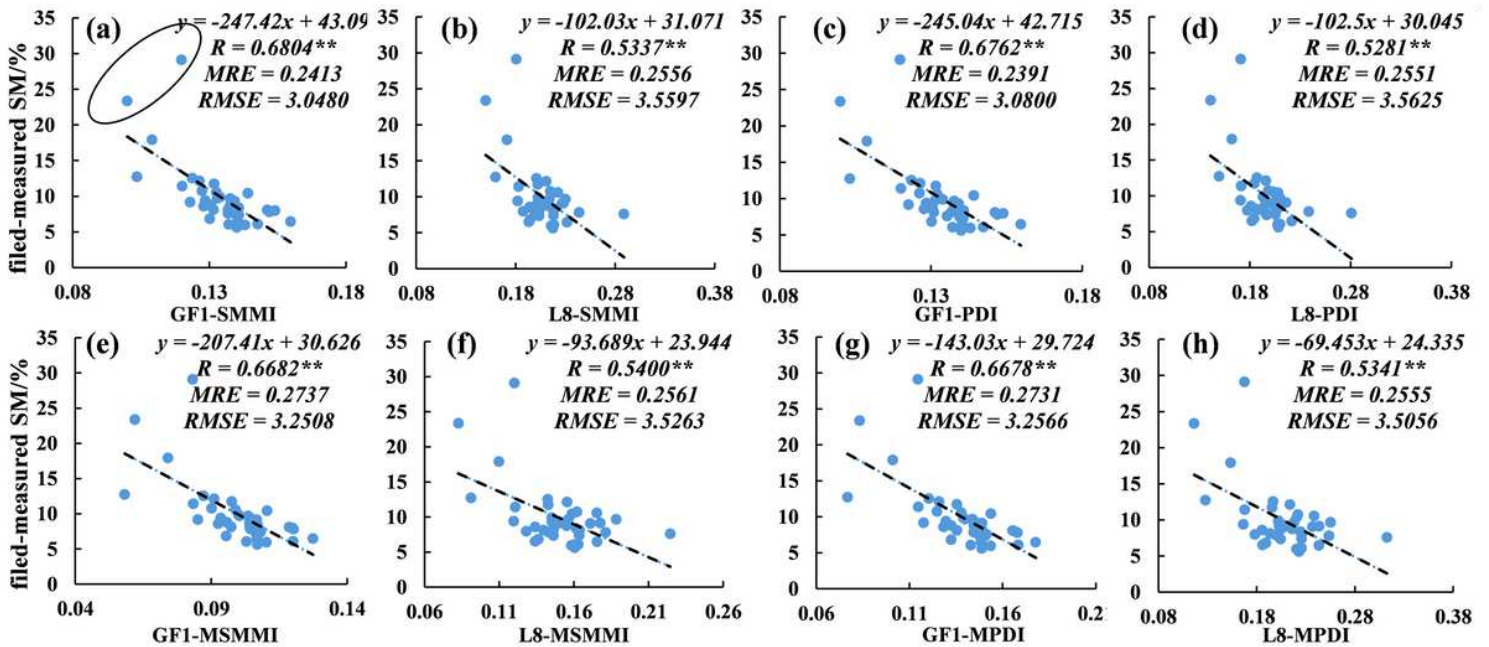


Figure 7

Relationship between four indicators and FSM in 10cm depth. (a) GF1-SMMI and FSM. (b) L8-SMMI and FSM (c) GF1-PDI and FSM. (d) L8-PDI and FSM. (e) GF1-MSMMI and FSM. (f) L8-MSMMI and FSM. (g) GF1-MPDI and FSM. (h) L8-MPDI and FSM.

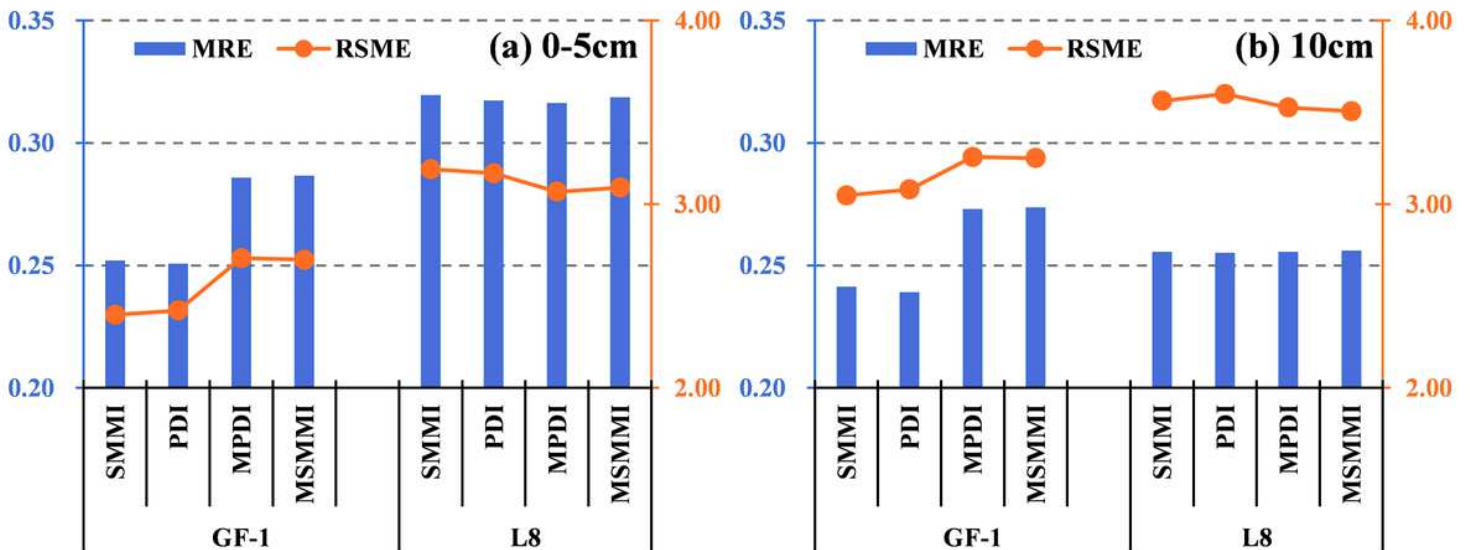
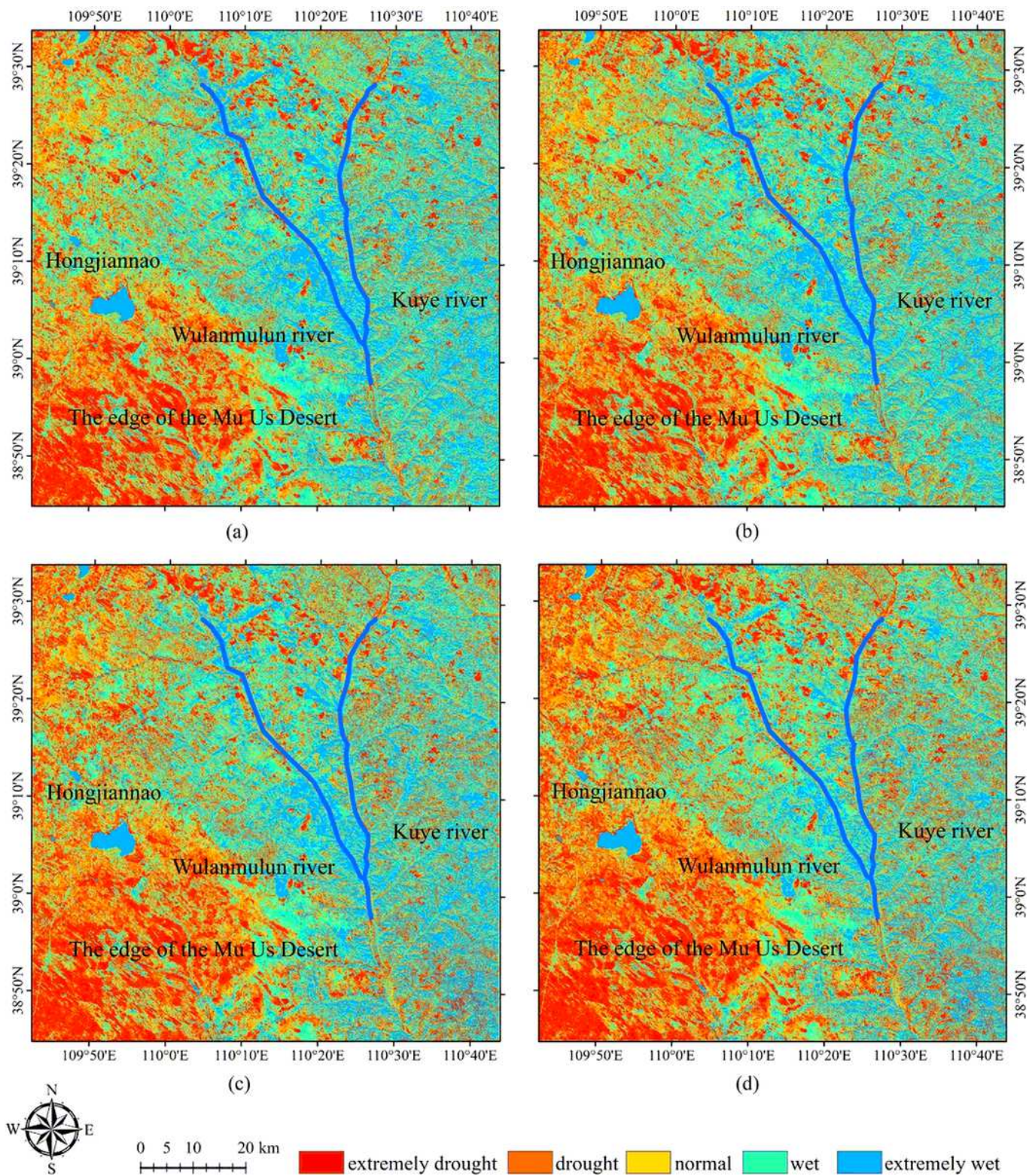


Figure 8

Accuracy of soil moisture estimation in 0-5cm and 10cm by GF-1 and L8.



**Figure 9**

The soil moisture map of GF-1. (a) SMMI. (b) PDI. (c) MSMMI. (d) MPDI. Note: The designations employed and the presentation of the material on this map do not imply the expression of any opinion whatsoever on the part of Research Square concerning the legal status of any country, territory, city or area or of its authorities, or concerning the delimitation of its frontiers or boundaries. This map has been provided by the authors.

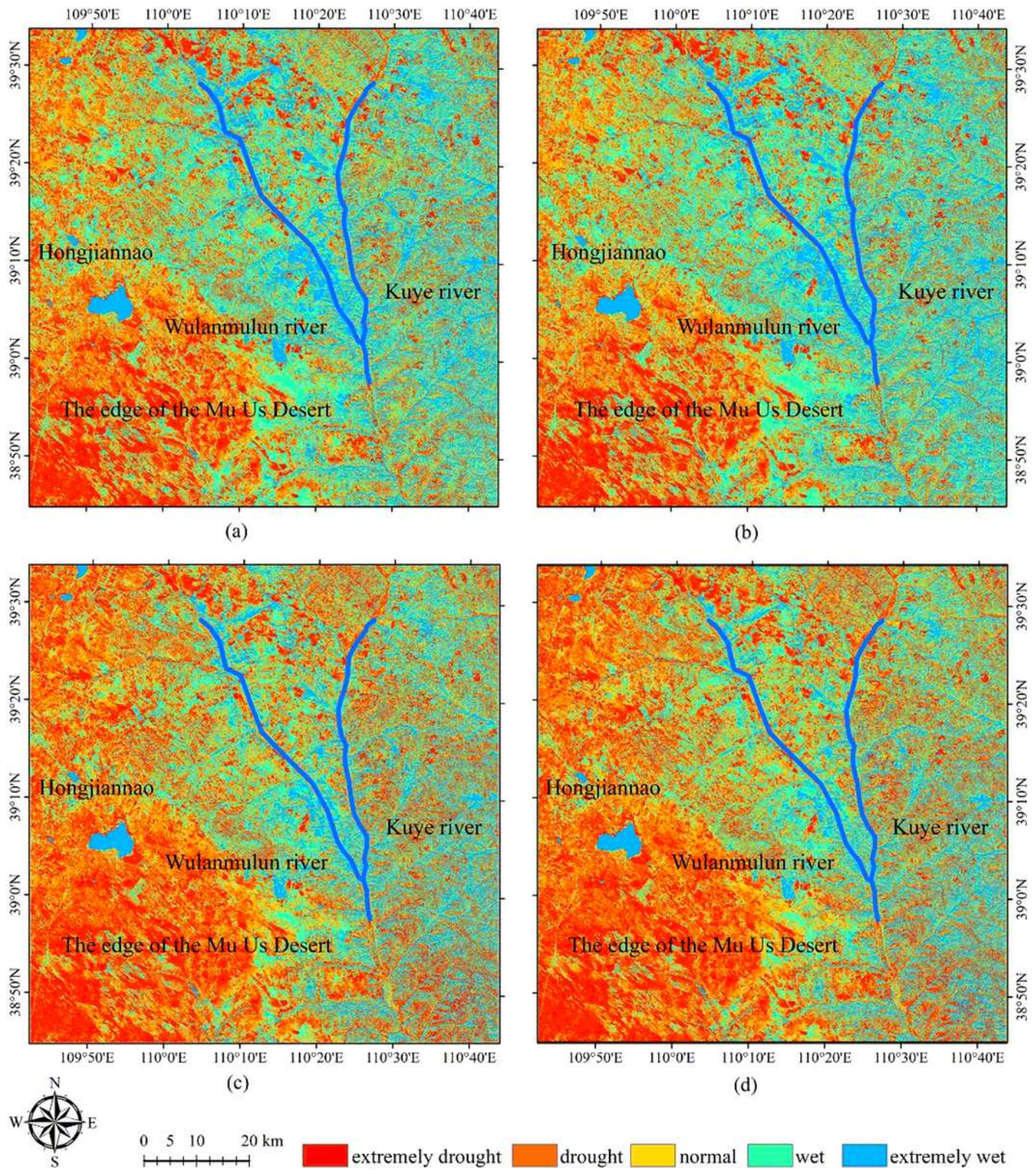


**Figure 10**

The soil moisture map of Landsat-8. (a) SMMI. (b) PDI. (c) MSMMI. (d) MPDI. Note: The designations employed and the presentation of the material on this map do not imply the expression of any opinion whatsoever on the part of Research Square concerning the legal status of any country, territory, city or area or of its authorities, or concerning the delimitation of its frontiers or boundaries. This map has been provided by the authors.

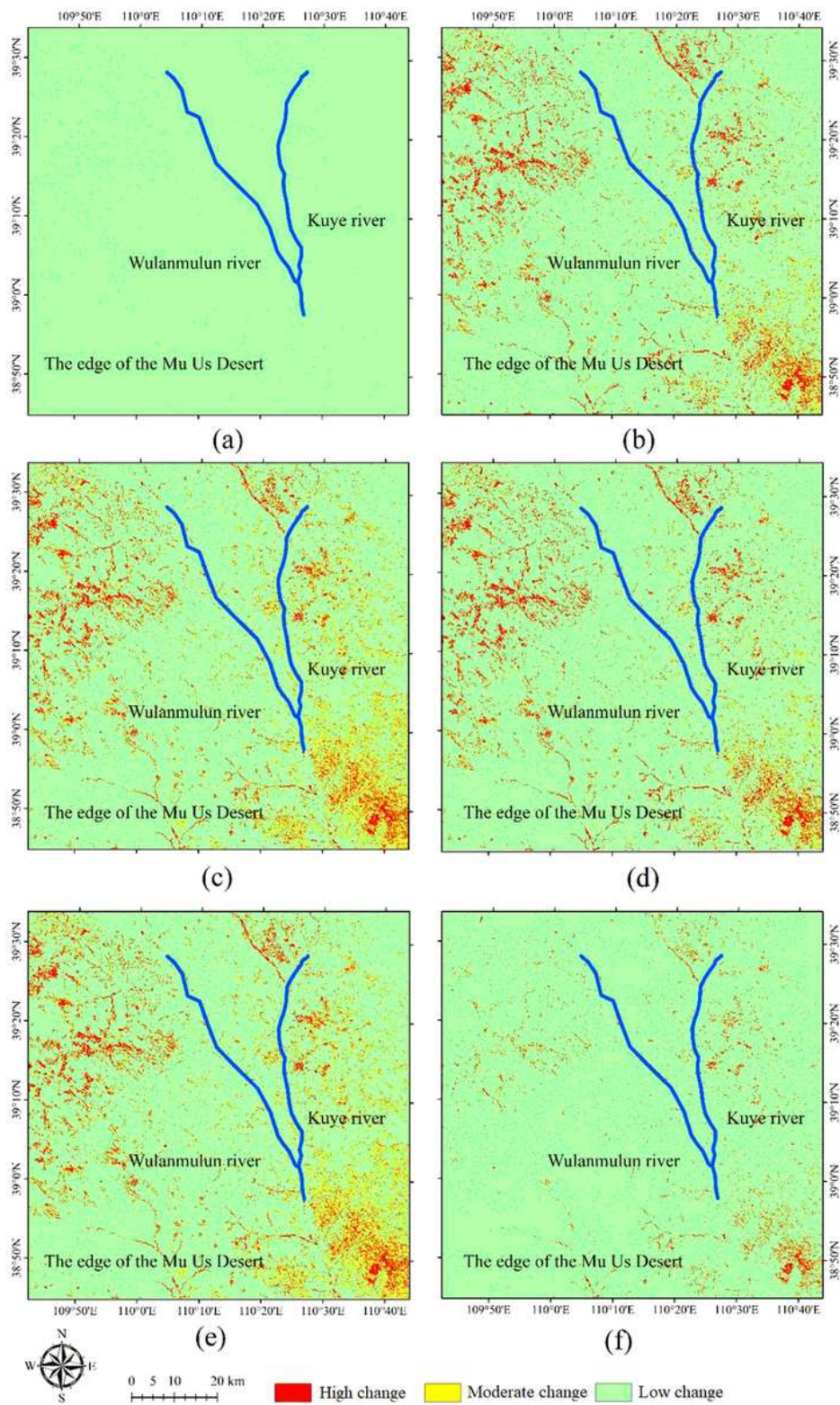


**Figure 11**

GSSIM map between four indicators of GF-1. (a) GSSIM between SMMI and PDI. (b) GSSIM between SMMI and MSMMI. (c) GSSIM between SMMI and MPDI. (d) GSSIM between PDI and MSMMI. (e) GSSIM between PDI and MPDI. (f) GSSIM between MPDI and MSMMI. Note: The designations employed and the presentation of the material on this map do not imply the expression of any opinion whatsoever on the part of Research Square concerning the legal status of any country, territory, city or area or of its

authorities, or concerning the delimitation of its frontiers or boundaries. This map has been provided by the authors.

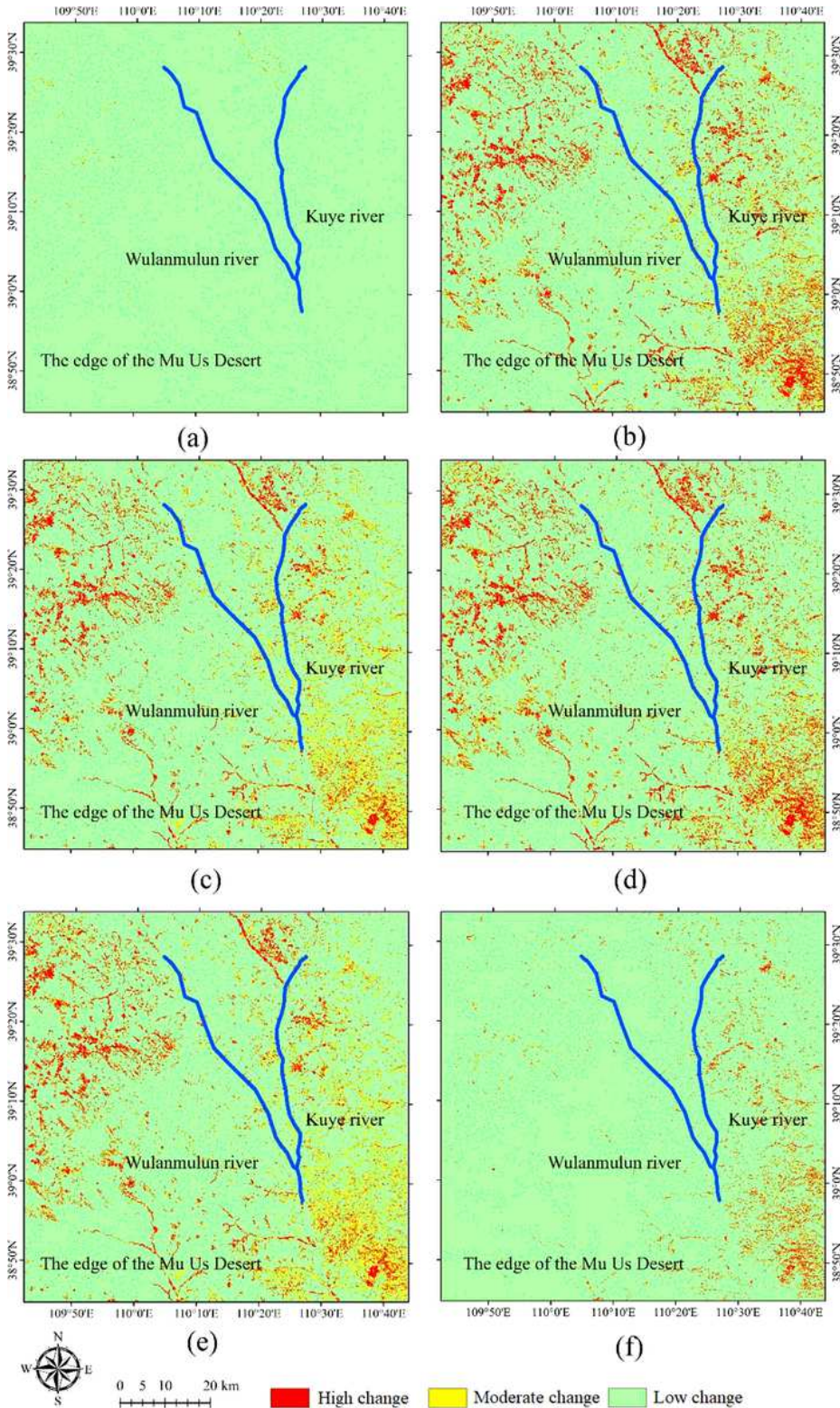


**Figure 12**

GSSIM map between four indicators of L8. (a) GSSIM between SMMI and PDI. (b) GSSIM between SMMI and MSMMI. (c) GSSIM between SMMI and MPDI. (d) GSSIM between PDI and MSMMI. (e) GSSIM between PDI and MPDI. (f) GSSIM between MPDI and MSMMI. Note: The designations employed and the

presentation of the material on this map do not imply the expression of any opinion whatsoever on the part of Research Square concerning the legal status of any country, territory, city or area or of its authorities, or concerning the delimitation of its frontiers or boundaries. This map has been provided by the authors.

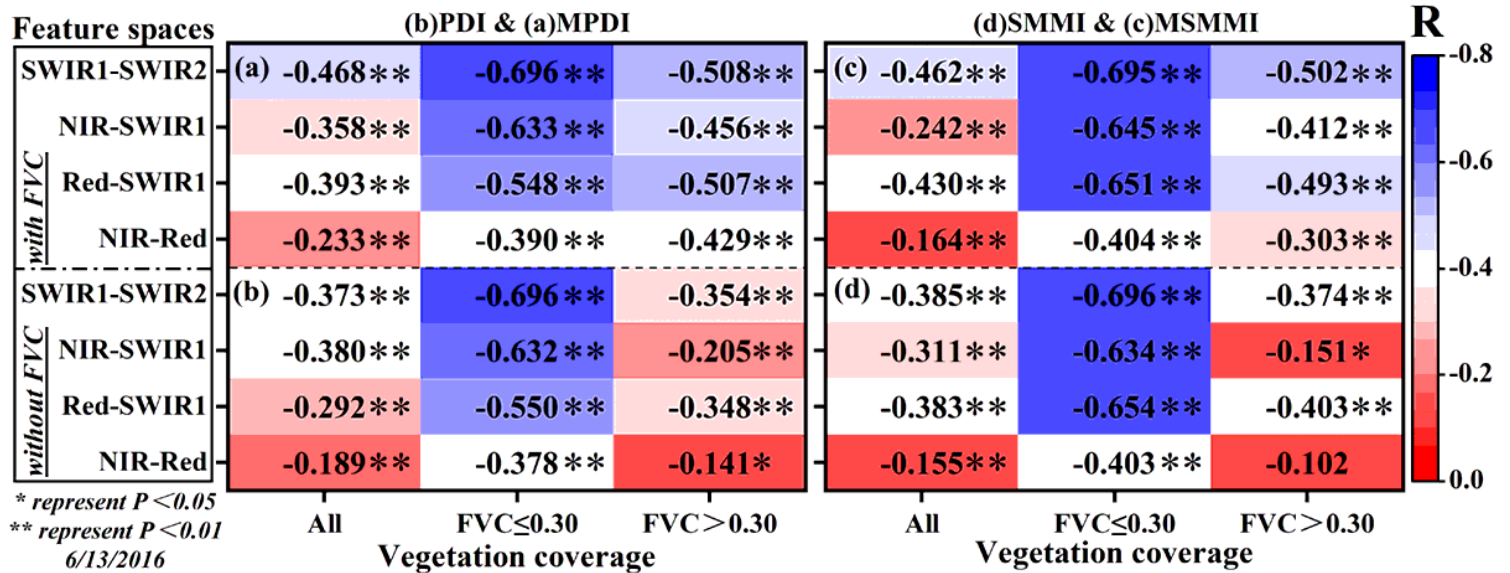


Figure 13

The relationship between measured SM and soil moisture indices under different land cover types from Sentinel-2 on June 13, 2016.

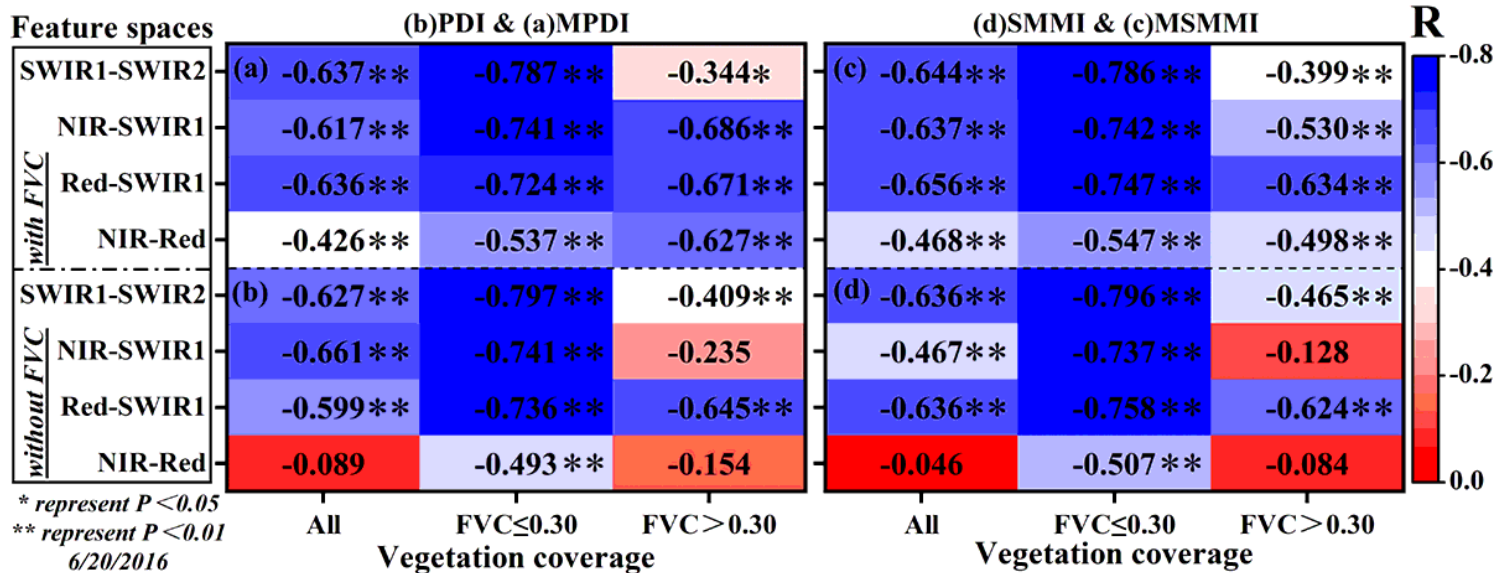


Figure 14

The relationship between measured SM and soil moisture indices under different land cover types by Sentinel-2 on June 20, 2016.

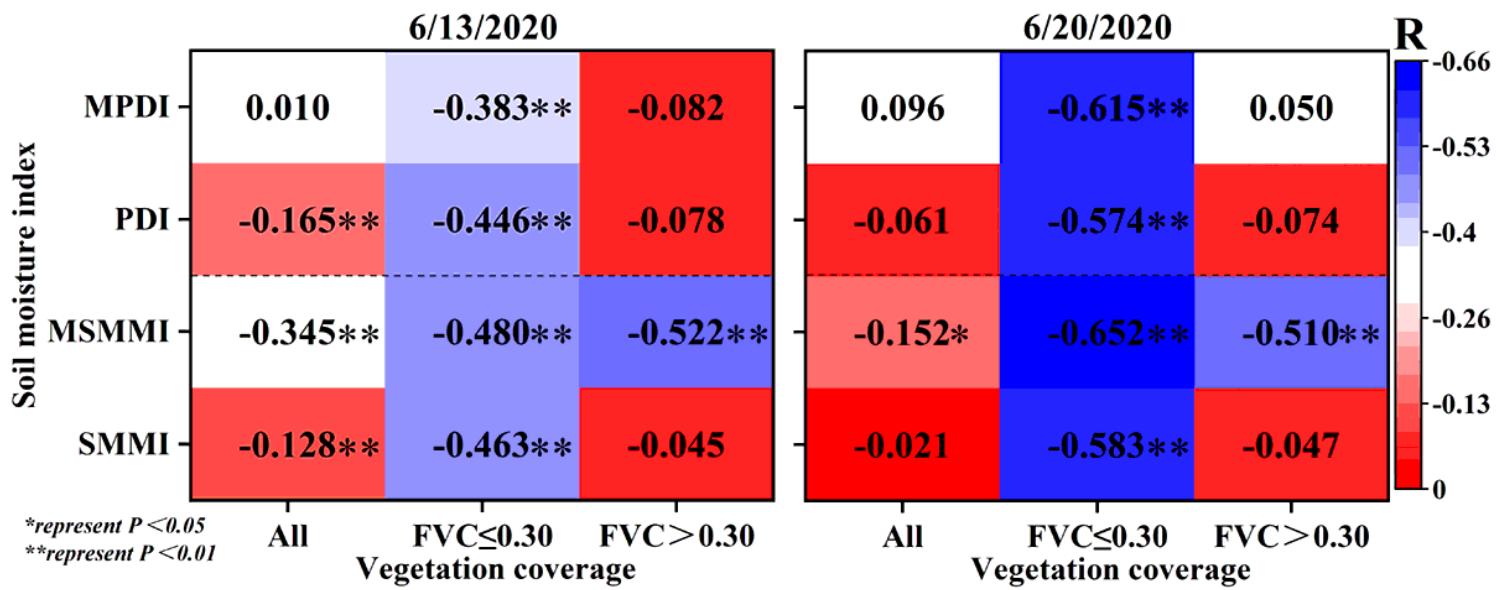
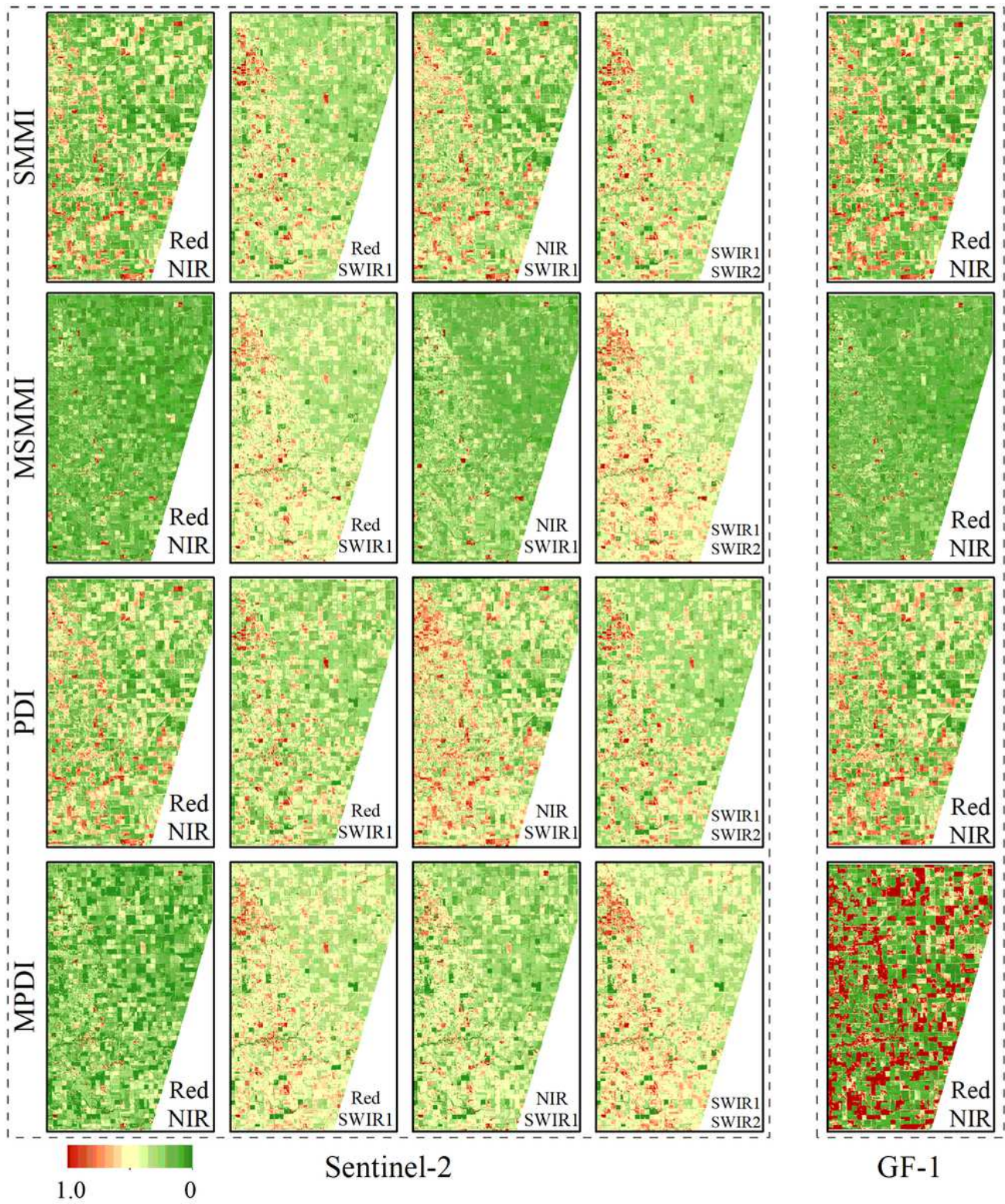


Figure 15

The relationship between measured SM and soil moisture indices under different land cover types by GF-1 on June 13 and June 20, 2016.



**Figure 16**

Spatial distribution of the four indices by Sentinel-2 and GF-1 on June 13, 2016.

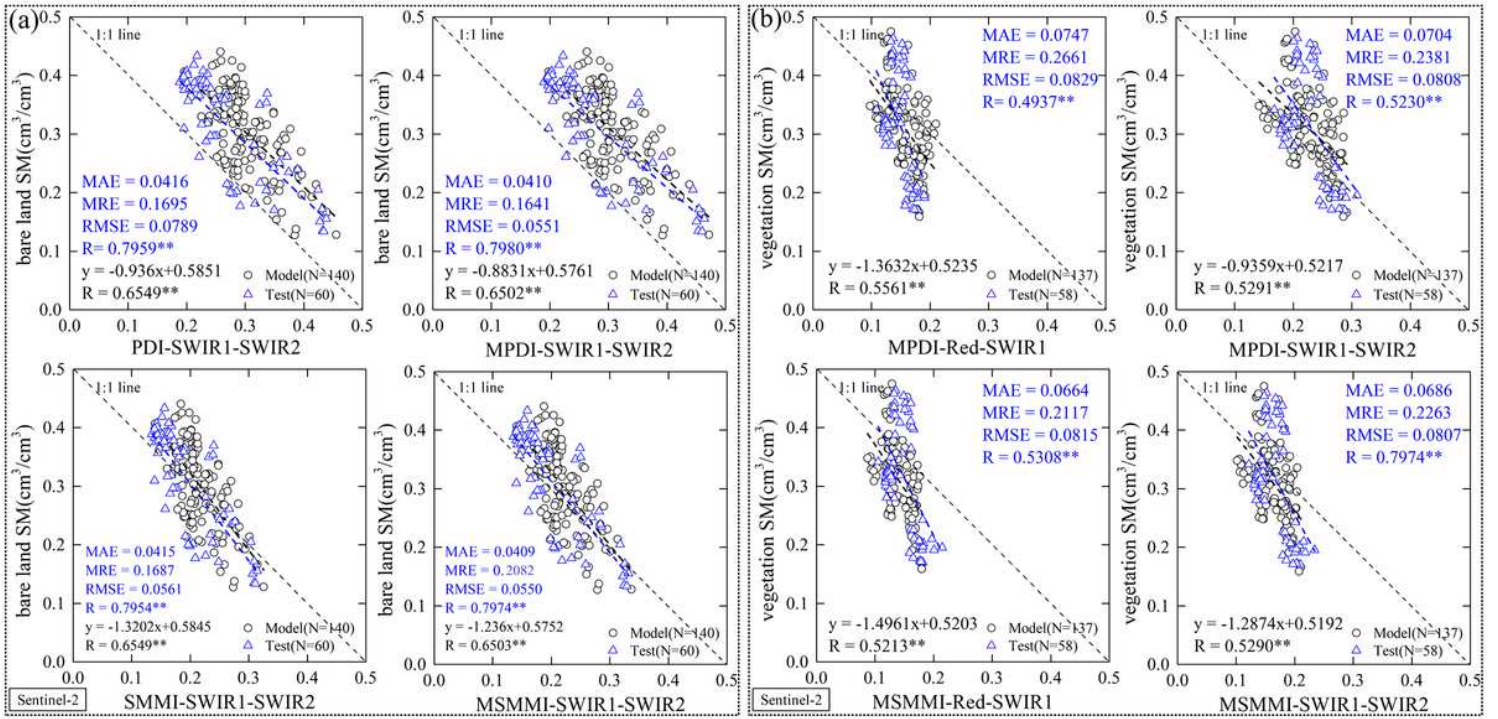


Figure 17

(a) The relationship among SMMI, PDI, MSMMI, MPDI, and SM in bare soil areas from SWIR1-SWIR2 space of Sentinel-2 on June 13, 2016. (b) The relationship among SMMI, PDI, MSMMI, MPDI, and SM in vegetation-covered areas from SWIR1-SWIR2 space of Sentinel-2 on June 13, 2016.

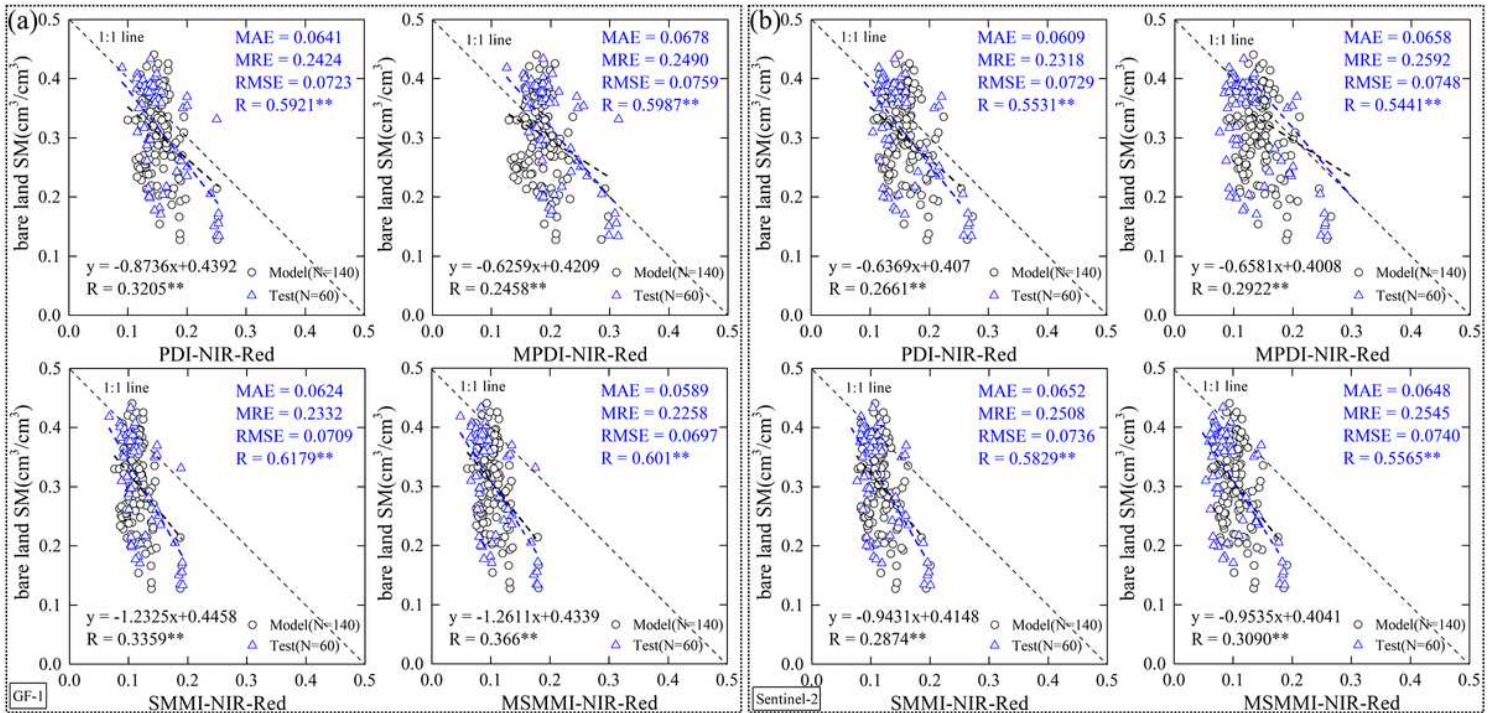


Figure 18

The relationship among SMMI, PDI, MSMMI, MPDI, and SM in bare soil areas from NIR-Red space on June 13, 2016. (a) GF-1, (b) Sentinel-2

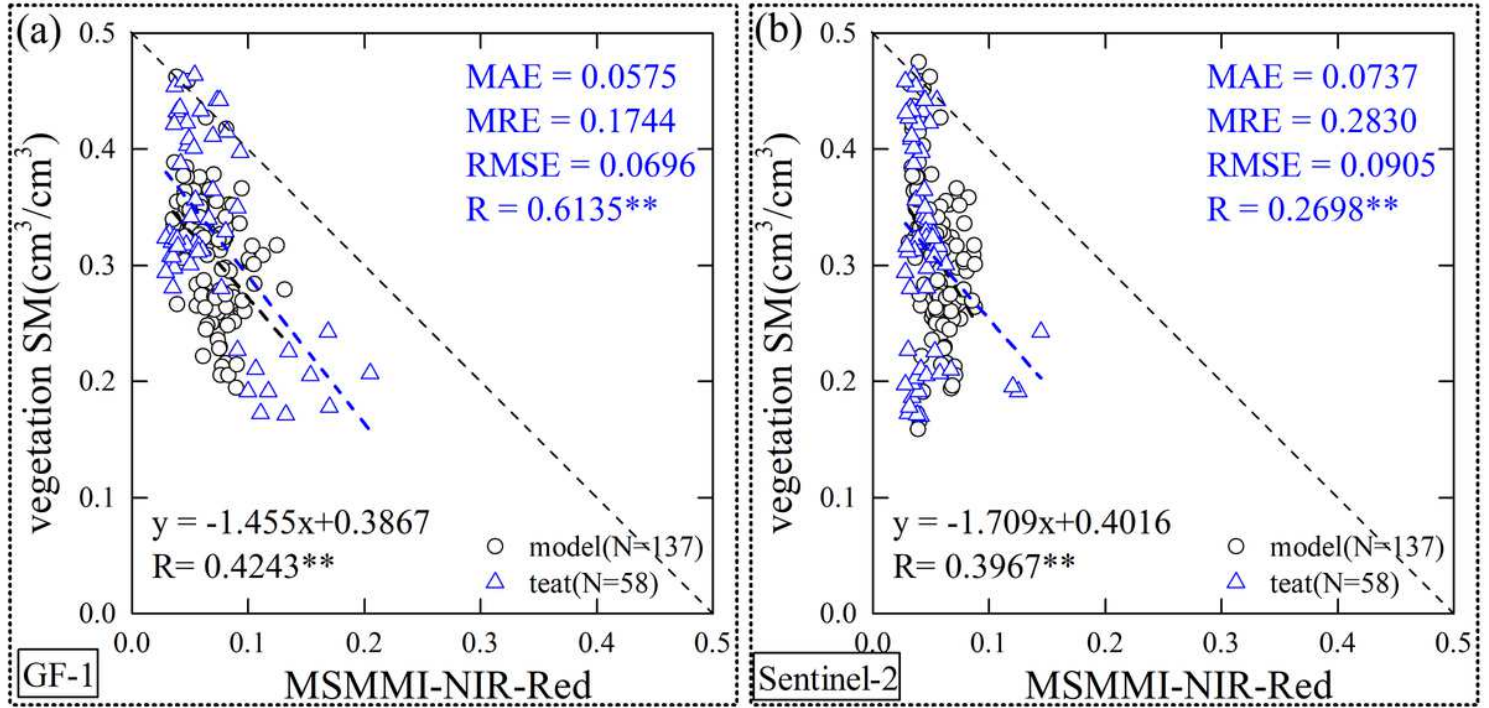


Figure 19

The relationship between MSMMI and SM in vegetation-covered areas from NIR-Red space on June 13, 2016.

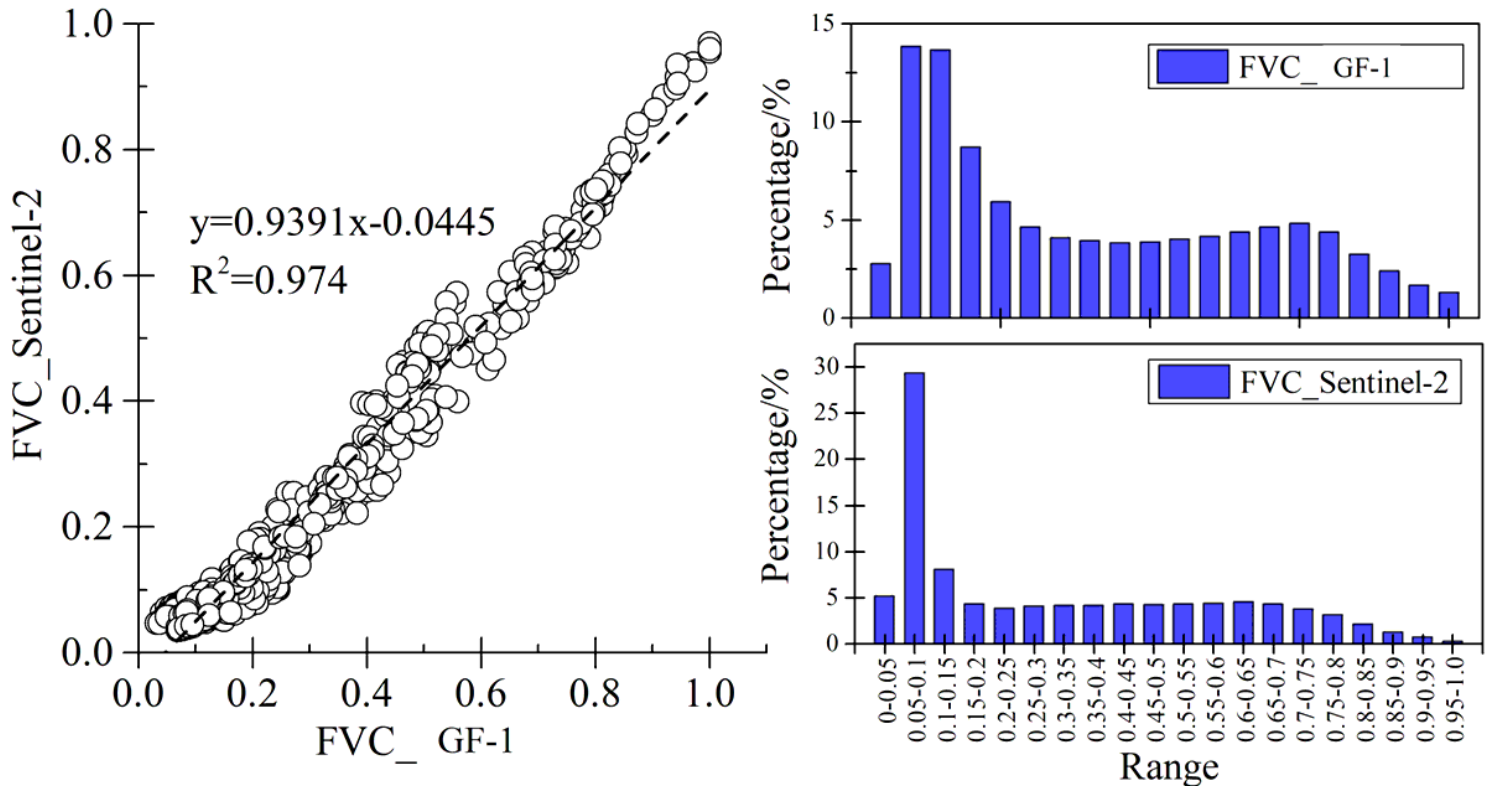


Figure 20

Correlation and histogram of two FVC methods on June 13, 2016

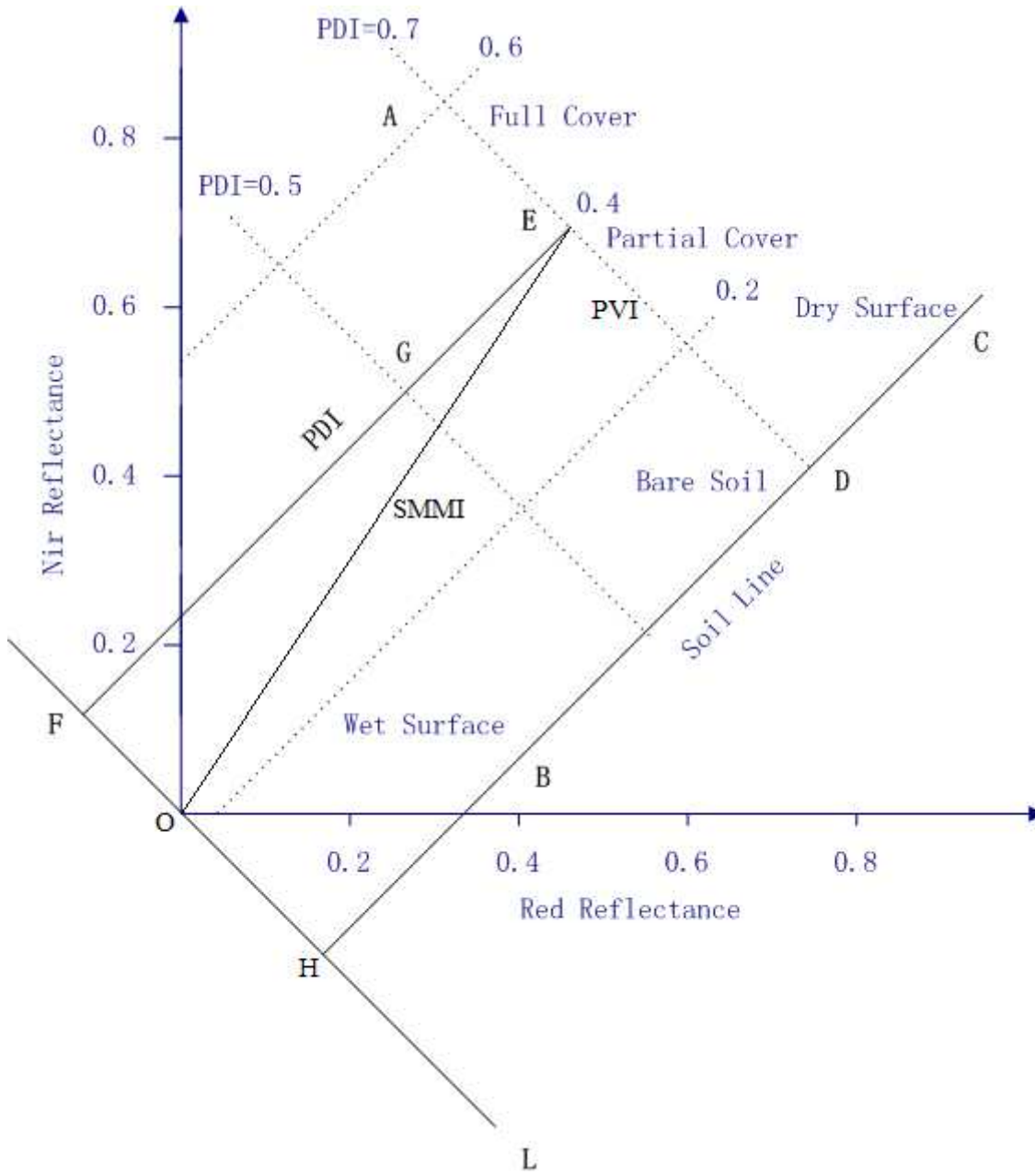


Figure 21

Relationship between PDI and SMMI.